Mon. Not. R. Astron. Soc. **350,** 485–505 (2004) doi:10.1111/j.1365-2966.2004.07659.x

Axisymmetric p-mode pulsations of stars with dipole magnetic fields

Hideyuki Saio[1]★ and Alfred Gautschy[2]

[1]*Astronomical Institute, Graduate School of Science, Tohoku University, Sendai, Miyagi 980-8578, Japan*
[2]*ETH-Library, Raemistr. 101, 8092 Zurich, Switzerland*

Accepted 2004 January 21. Received 2004 January 9; in original form 2003 November 7

ABSTRACT

The effect of a dipole magnetic field on adiabatic axisymmetric non-radial p-mode pulsations is studied numerically. The angular dependence of pulsation, which cannot be represented by a single spherical harmonic in the presence of a magnetic field, is expanded into a series of spherical harmonics with different degrees ℓ. The presence of a magnetic field not only shifts the pulsation frequency, the pulsations are also damped due to the generation of magnetic slow waves. In agreement with the results of Cunha & Gough, who used a different approach from ours, we find that the effect of a magnetic field on the intermediate-to-high-order p-modes is not monotonic but cyclic with respect to the pulsation frequency and the magnetic field strength. The damping rate of a high-order p-mode becomes very small at about 3 kG and 8 kG; the corresponding field strengths are higher for lower overtones. The diminished magnetic damping is favourable for the corresponding modes, if they are excited by the classical κ-mechanism, to survive even in the presence of a strong magnetic field. This picture could explain the mode selection as observed in the rapidly oscillating Ap stars. For a low-order p-mode, the damping rate increases as the strength of the magnetic field increases. We find that in the presence of a magnetic field of a few kG, magnetic damping seems to exceed the driving owing to the κ-mechanism of oscillations representative of δ Scuti variability. This may explain why δ Scuti-type oscillations are unlikely to be seen in magnetic Ap stars. The amplitude of a mainly dipole (or quadrupole) mode is strongly confined to the magnetic axis in the outer layers. Furthermore, horizontal motion can be comparable to radial motion even for high-order p-modes. We discuss the influence of the magnetic distortion of the eigenfunction on the pulsation amplitude modulation with respect to the rotation phase.

Key words: stars: chemically peculiar – stars: magnetic fields – stars: oscillations – stars: variables: other.

1 INTRODUCTION

Some magnetic Ap stars pulsate in high-order non-radial p-modes with periods between about 4 and 15 min. The class of variables is known as roAp (rapidly oscillating Ap) stars. Since 1982 when the first roAp variables were studied (Kurtz 1982), their number has increased to about 30. A thorough review of the observational properties and theoretical ideas underlying the peculiar oscillatory signatures of roAp stars was published by Kurtz (1990). Despite the success of the oblique pulsator model to describe roAp star pulsations, basic aspects remain to be understood. Concerning the excitation of oscillation modes, the hydrogen ionization zone was recently positively identified as being able to excite high-order p-modes in roAp stars (Dolez & Gough 1982; Dziembowski & Goode 1996; Gautschy, Saio & Harzenmoser 1998; Balmforth et al. 2001). The modelling of the excitation process did not, however, account for the strongly disturbing influence of the magnetic field in the superficial layers. Nevertheless, the case for partial hydrogen ionization to be responsible for driving the oscillations is a strong one.

A long-standing hope in the study of roAp stars is to use the observed pulsation frequencies for asteroseismological inferences (see, e.g. Matthews 1991, for a review). The classical stability analyses (neglecting magnetic fields completely) cannot account for the low number of observed modes that seem to be preferred in these stars. It is believed that the strong magnetic fields (of the order of some kG on the stellar surface) are essential in the process of mode selection. Furthermore, to determine theoretically the precise magnitude of the pulsation frequencies, the magnetic field must be accounted for. The coupling of pulsation with a stellar magnetic field constitutes, however, a formidable mathematical problem.

Biront et al. (1982) applied a singular perturbation method to a polytrope with a dipole magnetic field and obtained eigenfunctions for mainly radial pulsations. They concluded that the horizontal

★E-mail: saio@astr.tohoku.ac.jp

motion could become comparable to the radial motion close to the surface for pulsations that are mainly radial in the deep interior. This conclusion was objected to by Roberts & Soward (1983) who showed that the ratio of horizontal to radial displacements on the stellar surface is of order 1/10. Roberts & Soward (1983) found that inward-propagating slow waves are generated on the stellar surface. These waves have very short wavelengths in the deep interior of the star so that they are expected to dissipate before they reach the centre; i.e. the slow waves constitute a sink of the pulsation energy.

Dziembowski & Goode (1996) were the first to study axisymmetric high-order low-degree p-modes in the presence of a dipole magnetic field. They solved the perturbation equations for magnetic and mechanical variables in a thin surface zone, neglecting the angular derivatives of the perturbed quantities for simplicity. At the bottom of the surface zone, the superficial solution was used as the outer boundary condition for the interior problem where the acoustic oscillations were assumed to decouple completely from the magnetic oscillations. Bigot et al. (2000) extended this method to non-axisymmetric modes. They have shown that kG magnetic fields shift oscillation frequencies by 10–20 μHz and modify significantly the latitudinal dependence of the surface amplitude.

Cunha & Gough (2000) approached the roAp problem using a variational principle with an asymptotic theory for high-order p-mode oscillations. They used a local approximation in the surface boundary layer where the coupling between acoustic and magnetic oscillations is important. Cunha & Gough applied their method to a polytrope and found that for a given magnetic field strength the frequency shift shows steep changes at specific frequencies. At the locations of the steep frequency shifts, the damping rate peaks sharply.

We note that the generation of slow magnetoacoustic waves (slow waves) is also considered as a mechanism for the observed absorption of solar p-mode oscillations in sunspots (e.g. Spruit & Bogdan 1992; Cally & Bogdan 1993). Although a plane-parallel structure with vertical magnetic fields was used in their studies, some of their results are similar to our results for a spherical model with a dipole magnetic field.

In this paper, we solve the equations for adiabatic axisymmetric oscillations that couple with a dipole magnetic field. We adopt a method somewhat different from those used hitherto. We expand the latitudinal variation of the eigenfunctions into spherical harmonics, which is in common with the Dziembowski & Goode (1996) method. However, instead of solving the equations separately for the thin surface zone, we solve the full equations (as a truncated series), including magnetic and acoustic variables. We adopt running-wave conditions at the bottom of a thin surface zone for magnetic variables, while we apply the usual central boundary conditions to the acoustic variables at the centre. We discuss the basic equations in Section 2 and the method of numerical calculations in Section 3. The details of the equations for the numerical analysis are given in Appendix B. The unperturbed models used are described in Section 4. The results are presented in Section 5 and finally discussed in Section 6. In Appendix A, basic properties of the magnetohydrodynamic (MHD) equations, based on a local analysis, are discussed.

2 BASIC EQUATIONS

In the following analysis of non-radial pulsations, we disregard stellar rotation and assume that the unperturbed magnetic field $\boldsymbol{B}_0$ is a dipole that can be expressed as

$$\boldsymbol{B}_0 = \frac{B_{\rm p}}{(r/R)^3}\left(\boldsymbol{e}_r\cos\theta + \boldsymbol{e}_\theta\frac{1}{2}\sin\theta\right), \tag{1}$$

where r is the distance from the stellar centre, θ is the co-latitude with respect to the magnetic axis (which is the axis of symmetry) and $\boldsymbol{e}_r$ and $\boldsymbol{e}_\theta$ are unit vectors in the radial and θ directions respectively. The stellar radius is denoted as R, and $B_{\rm p}$ represents the surface polar field strength. (Equation 1 is singular at the centre. We use the equation nonetheless as we need it for the outer part of the stellar interior.) A dipole field is a potential field, which is force free, so we assume that the unperturbed stellar structure is spherically symmetric. (We disregard in this paper the effect of the magnetic field on convective flux.)

We perturb the equations governing the material motion in the stellar interior, adopting ideal magnetohydrodynamics with infinite conductivity and Cowling's approximation. The temporal dependence of the perturbed quantities is expressed as $\exp(\mathrm{i}\sigma t)$. Then, the linearized equations for adiabatic non-radial pulsations (e.g. Unno et al. 1989) are

$$-\sigma^2\boldsymbol{\xi} = \frac{\rho'}{\rho^2}\frac{{\rm d}p}{{\rm d}r}\boldsymbol{e}_r - \frac{1}{\rho}\nabla p' + \frac{1}{4\pi\rho}(\nabla\times\boldsymbol{B}')\times\boldsymbol{B}_0, \tag{2}$$

$$\rho' = -\nabla\cdot(\rho\boldsymbol{\xi}), \tag{3}$$

$$\boldsymbol{B}' = \nabla\times(\boldsymbol{\xi}\times\boldsymbol{B}_0), \tag{4}$$

$$\frac{p'}{p} = \Gamma_1\frac{\rho'}{\rho} + \Gamma_1 A\xi_r, \tag{5}$$

where $\boldsymbol{\xi}$ is the displacement vector, ρ the unperturbed density, and p the unperturbed pressure. The dash indicates the Eulerian perturbation of a physical quantity. We have used

$$A = \frac{{\rm d}\ln\rho}{{\rm d}r} - \frac{1}{\Gamma_1}\frac{{\rm d}\ln p}{{\rm d}r} \quad\text{and}\quad \Gamma_1 = \left(\frac{{\rm d}\ln p}{{\rm d}\ln\rho}\right)_{\rm ad}. \tag{6}$$

At the outer boundary we impose mechanical and magnetic outer boundary conditions. The mechanical condition is derived from the requirement that $|\partial/\partial r(\delta p/p)|$ remains finite as $p\to 0$ (Cox 1980), where δp is the Lagrangian perturbation of pressure. The magnetic boundary condition is

$$\nabla\times\boldsymbol{B}' = 0, \tag{7}$$

which means that the magnetic field should approach a source-free potential field outside of the star. Roberts & Soward (1983) showed that slow magnetic waves are generated and propagate toward the centre. Before being reflected in the centre, the slow waves are expected to be dissipated due to their very short spatial wavelengths deep in the star. To take account of this effect, we impose a running wave condition for magnetic field perturbations on a sphere with $r = r_{\rm b}$ ($\geqslant 0.95R$). In the deeper interior ($r < r_{\rm b}$), we neglect the interaction between magnetic field and pulsation (see below and Appendix B for details). At the stellar centre, we apply the usual mechanical condition (Cox 1980; Unno et al. 1989).

With these boundary conditions, equations (2)–(5) pose an eigenvalue problem for the eigenvalue σ. The eigenvalues are complex because of the leak of pulsation energy into the stellar interior, carried away by the running slow waves.

3 METHOD OF NUMERICAL CALCULATION

In the presence of a magnetic field, the angular dependence of non-radial pulsations can no longer be represented by a single spherical harmonic. Therefore, we adopt an expansion in a series of spherical harmonics Y_ℓ^m. The method is conceptually the same as the one describing non-radial pulsations in rotating stars (see Section 34 in

Unno et al. 1989, and references therein). The above equations lead to a coupling of terms of different ℓ and therefore to an infinite set of coupled differential equations. To reduce the complexity of the problem, we consider in this paper only axisymmetric, i.e. $m = 0$, modes. For these modes, the corresponding vector fields $\boldsymbol{\xi}$ and $\boldsymbol{B}'$ can be expanded on a sphere as

$$\boldsymbol{\xi} = \sum_{\ell} \left(\xi_{r\ell} Y_\ell^0 \boldsymbol{e}_r + \xi_{\mathrm{p}\ell} \frac{\mathrm{d}Y_\ell^0}{\mathrm{d}\theta} \boldsymbol{e}_\theta \right), \tag{8}$$

$$\boldsymbol{B}' = \sum_{\ell} \left(b_{r\ell} Y_\ell^0 \boldsymbol{e}_r + b_{\mathrm{p}\ell} \frac{\mathrm{d}Y_\ell^0}{\mathrm{d}\theta} \boldsymbol{e}_\theta \right). \tag{9}$$

Perturbed scalar quantities are expanded as

$$f' = \sum_{\ell} f'_\ell Y_\ell^0, \tag{10}$$

where Y_ℓ^0 stands for spherical harmonics with $m = 0$. The restriction of our computations to axisymmetric modes makes toroidal terms unnecessary in equations (8) and (9) and hence simplifies the system of equations considerably.

We use the following dependent variables:

$$\begin{aligned} y_{1,\ell} &= \frac{\xi_{r\ell}}{r}, & y_{2,\ell} &= \frac{p'_\ell}{\rho g r}, \\ y_{3,\ell} &= \frac{\omega^2 \xi_{\mathrm{p}\ell}}{r} - y_{2,\ell}, & y_{4,\ell} &= \frac{x^3 b_{\mathrm{p}\ell}}{B_{\mathrm{p}}}, \end{aligned} \tag{11}$$

where ω is the angular frequency of pulsation normalized as

$$\omega = \frac{\sigma}{\sqrt{GM/R^3}}. \tag{12}$$

The variables $y_{1,\ell}$ and $y_{2,\ell}$ are the canonical ones used in computing non-radial pulsations, while $y_{3,\ell}$ is proportional to the horizontal displacement caused by the presence of a magnetic field, and $y_{4,\ell}$ is proportional to the horizontal perturbation of the magnetic field. The governing equations are separated into two independent infinite systems of coupled differential equations. One involves

$$y_{1,\ell}, \quad y_{2,\ell}, \quad y_{3,\ell}, \quad y_{4,l+1}$$

with

$$\ell = 2j - 1 \quad \text{for} \quad j = 1, 2, \ldots \quad \text{odd modes.} \tag{13}$$

The other system consists of the same variables but with

$$\ell = 2j - 2 \quad \text{for} \quad j = 1, 2, \ldots \quad \text{even modes.} \tag{14}$$

In the numerical computation, the series have to be truncated at some j. Details of the adopted numerical strategy to solve the truncated system of equations are given in Appendix B.

The strength of the magnetic field enters the equations via the quantity

$$\eta \equiv \frac{B_{\mathrm{p}}^2}{8\pi p} \left(\frac{R}{r} \right)^6 \frac{H_{\mathrm{p}}}{r}, \tag{15}$$

where H_{p} stands for the pressure scaleheight. The variable η, being proportional to the ratio of the magnetic energy density to the local gravitational potential energy, decreases towards the stellar interior (Fig. 2 below).

Due to the generation of *slow waves* (Roberts & Soward 1983), variables y_3 and y_4 oscillate rapidly in the deeper stellar envelope. The wavelength, λ_{s}, can be estimated as

$$\frac{\lambda_{\mathrm{s}}}{r} \sim \frac{2\pi v_{\mathrm{A}}/r}{\sigma} \sim \frac{3\pi\sqrt{\eta}}{\omega} \tag{16}$$

with v_{A} being the Alfvén speed (see, e.g. Appendix A). The radial wavelength, λ_{p}, of a high-order p-mode of low latitudinal degree is approximately $2\pi c_{\mathrm{s}}/\sigma$, where c_{s} is the adiabatic sound speed. Therefore,

$$\lambda_{\mathrm{s}}/\lambda_{\mathrm{p}} \simeq v_{\mathrm{A}}/c_{\mathrm{s}}. \tag{17}$$

Hence, the slow waves decouple from the p-mode pulsation when the Alfvén speed is much lower than the sound speed.

Inward-propagating waves with very short wavelengths are expected to be dissipated before they reach the centre of the star (Roberts & Soward 1983). Therefore, running wave conditions for $y_{3,\ell}$ and $y_{4,\ell}$ are imposed at $r = r_{\mathrm{b}}$ where $\lambda_{\mathrm{s}} \ll H_{\mathrm{p}}$ and $\lambda_{\mathrm{s}} \ll \lambda_{\mathrm{p}}$. For $r < r_{\mathrm{b}}$, only the differential equations for $y_{1,\ell}$ and $y_{2,\ell}$ are solved. We checked the sensitivity of eigenvalues on the choice of r_{b}. As will be shown in Section 5.2.1 below, the eigenvalues are insensitive to the choice of r_{b} whenever the expansion method converges well.

To compute eigensolutions, we solved $4 \times n_{\mathrm{c}}$ (n_{c} is the number of ℓ-components included) first-order differential equations for complex variables. The differential equations were discretized into a set of difference equations. The complex eigenvalues and eigenfunctions were obtained with a relaxation method. For sufficient resolution, the interior of an equilibrium model is discretized into 7000 shells. Most of the grid points are located in the layers of $r/R > 0.95$. Such a high-density grid is necessary to resolve short-wavelength spatial oscillations in y_3, y_4.

4 MODEL STARS

We have obtained eigenfrequencies and eigenfunctions of two model stars of 1.7 $\mathrm{M}_\odot$ for various magnetic field strengths. The model parameters are listed in Table 1. We have adopted an initial composition of $(X, Z) = (0.70, 0.02)$ for the computation of evolutionary models. For the opacities, we referred to the OPAL95 (Iglesias & Rogers 1996) tables. We have adopted the T–τ relation given in Gautschy et al. (1998) without temperature inversion for the unperturbed temperature distribution above the photosphere. Model 1 is on the zero-age main sequence (ZAMS) while Model 2 is slightly evolved. For comparison with previous computations we have additionally obtained eigenfrequencies of an $n = 3$ polytrope whose mass and radius are scaled to 2 $\mathrm{M}_\odot$ and 2 $\mathrm{R}_\odot$, respectively.

A propagation diagram for Model 1 is depicted in Fig. 1; it shows the run of the Brunt–Väisälä frequency N and of the Lamb frequency L_ℓ for $\ell = 1$. The quantities N^2 and L_ℓ^2 are defined as

$$N^2 = -gA \quad \text{and} \quad L_\ell^2 = \frac{\ell(\ell+1)c_{\mathrm{s}}^2}{r^2}, \tag{18}$$

with g being the gravitational acceleration, A the Schwarzschild discriminant given in equation (6), and c_{s} the adiabatic sound speed.

Table 1. Model parameters.

Model	$M/\mathrm{M}_\odot$	$R/\mathrm{R}_\odot$	$\log T_{\mathrm{eff}}$	$\log L/\mathrm{L}_\odot$	X_{c}	$\sqrt{GM/R^3}/(2\pi)$ (mHz)
1...	1.7	1.517	3.895	0.896	0.70	6.96×10^{-2}
2...	1.7	1.986	3.861	0.993	0.35	4.65×10^{-2}

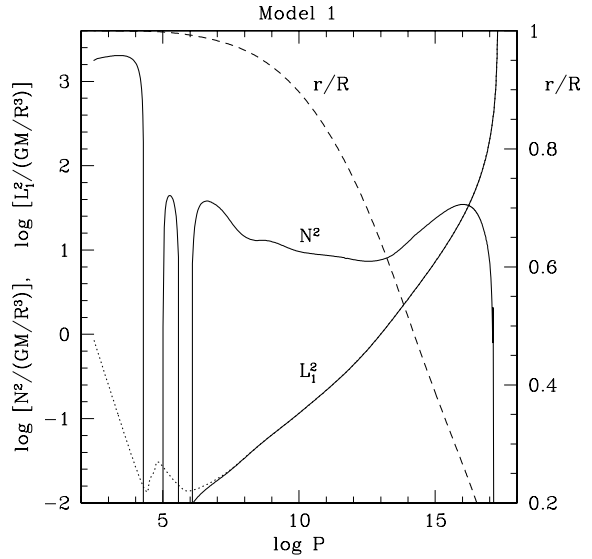

Figure 1. A propagation diagram for the unperturbed model with 1.7 $M_\odot$ on the ZAMS (Model 1). The p-mode critical frequency lies at $\omega = 47.3$ (3.3 mHz). The dashed line gives the relation between r/R and $\log P$; the corresponding scale is shown on the right-hand side. The dotted line shows the spatial variation of the square of modified Lamb frequency, $\ell(\ell+1)(c_s^2 + v_A^2)/r^2$, with $\ell = 1$ for $B_p = 3$ kG.

The phase speed of the fast magnetoacoustic waves is given as $\sqrt{c_s^2 + v_A^2}$ (e.g. Appendix A) with v_A being the Alfvén speed. A modified Lamb frequency that is associated with the speed of the fast wave may be defined as

$$L_\ell'^2 = \frac{\ell(\ell+1)\left(c_s^2 + v_A^2\right)}{r^2}. \tag{19}$$

The run of the modified Lamb frequency for $\ell = 1$ is also plotted in Fig. 1 by a dotted line for $B_p = 3$ kG. As seen in this figure, the Brunt–Väisälä frequency in the outermost layer is much larger than the modified Lamb frequency for a magnetic field strength of a few kG. This means that the outer turning point for the oscillation modes considered in this paper is governed by the Brunt–Väisälä frequency (as in the absence of a magnetic field) rather than the modified Lamb frequency. The p-mode critical frequency for Model 1 is about $\omega = 47.3$ (3.3 mHz). All the pulsation modes computed in this paper have frequencies below the critical frequency.

Our 1.7-$M_\odot$ models have two thin convective zones caused by H, He and He^+ ionization. The structure of convective zones is calculated with a local mixing-length theory with the mixing length set to be $1.5H_p$. The dashed line in Fig. 1 shows the relation between the fractional radius and pressure. The photosphere lies at $\log P = 4.423$. The optical depth at the outermost grid point of the computations is 0.002.

The model stars lie within the δ Sct instability region on the Hertzsprung–Russell diagram. Some of the non-adiabatic properties of low-order pulsations of radial and dipole modes obtained neglecting the effect of magnetic field are listed in Table 2, where we list cyclic frequencies ν, the real parts of normalized eigenfrequencies, ω_r, and the ratio of the imaginary to the real parts of the eigenfrequencies, ω_i/ω_r. The growth/damping times are given in units of seconds. A pulsation mode with a negative ω_i is pulsationally unstable (overstable). Table 2 indicates that some low-order radial and dipole modes, representative for δ Sct-type pulsations, are overstable.

The magnetic field strength enters the equations via the parameter η defined in equation (15). The full lines in Fig. 2 show η and the ratio of the Alfvén to the sound speed for $B_p = 1$ kG as well as the density distribution in the envelope of Model 1. For comparison, the same physical variables in the polytropic model are shown by dashed curves. Notice that the quantity η is always much smaller

Table 2. Non-adiabatic pulsations of the non-magnetic 1.7-$M_\odot$ models.

Model 1

		$\ell = 0$					$\ell = 1$		
k	ν (mHz)	ω_r	$-\omega_i/\omega_r$	$1/\tau_g$ (s)	k	ν (mHz)	ω_r	$-\omega_i/\omega_r$	$1/\tau_g$ (s)
0	0.248	3.56	2.8×10^{-8}	4.3×10^{-11}	1	0.316	4.55	-3.3×10^{-8}	-6.5×10^{-11}
1	0.320	4.59	3.3×10^{-7}	6.7×10^{-10}	2	0.369	5.31	4.3×10^{-8}	1.0×10^{-10}
2	0.389	5.58	1.5×10^{-6}	3.7×10^{-9}	3	0.439	6.31	7.8×10^{-7}	2.2×10^{-9}
3	0.460	6.61	5.8×10^{-6}	1.7×10^{-8}	4	0.519	7.45	3.4×10^{-6}	1.1×10^{-8}
4	0.537	7.72	1.8×10^{-5}	6.2×10^{-8}	5	0.601	8.63	7.4×10^{-6}	2.8×10^{-8}
5	0.618	8.88	4.7×10^{-5}	1.8×10^{-7}	6	0.683	9.82	1.4×10^{-6}	6.1×10^{-9}
6	0.700	10.1	9.8×10^{-5}	4.3×10^{-7}	7	0.764	11.0	-5.4×10^{-5}	-2.6×10^{-7}
7	0.782	11.2	1.4×10^{-4}	7.1×10^{-7}	8	0.845	12.1	-2.2×10^{-4}	-1.2×10^{-6}
8	0.863	12.4	1.1×10^{-4}	5.7×10^{-7}	9	0.926	13.3	-5.1×10^{-4}	-3.0×10^{-6}
9	0.945	13.6	-7.4×10^{-5}	-4.4×10^{-7}	10	1.008	14.5	-8.8×10^{-4}	-5.6×10^{-6}

Model 2

		$\ell = 0$					$\ell = 1$		
k	ν (mHz)	ω_r	$-\omega_i/\omega_r$	$1/\tau_g$ (s)	k	ν (mHz)	ω_r	$-\omega_i/\omega_r$	$1/\tau_g$ (s)
0	0.165	3.55	2.1×10^{-7}	2.2×10^{-10}	1	0.244	5.25	4.6×10^{-6}	7.1×10^{-9}
1	0.214	4.59	1.9×10^{-6}	2.5×10^{-9}	2	0.280	6.02	2.0×10^{-5}	3.5×10^{-8}
2	0.265	5.69	8.0×10^{-6}	1.3×10^{-8}	3	0.320	6.87	4.2×10^{-5}	8.5×10^{-8}
3	0.315	6.78	2.5×10^{-5}	4.9×10^{-8}	4	0.358	7.70	1.1×10^{-4}	2.5×10^{-7}
4	0.366	7.88	6.6×10^{-5}	1.5×10^{-7}	5	0.406	8.74	3.1×10^{-4}	7.8×10^{-7}
5	0.419	9.00	1.5×10^{-4}	4.0×10^{-7}	6	0.459	9.86	6.5×10^{-4}	1.9×10^{-6}
6	0.471	10.1	2.7×10^{-4}	8.1×10^{-7}	7	0.512	11.0	1.0×10^{-3}	3.3×10^{-6}
7	0.524	11.3	3.4×10^{-4}	1.1×10^{-6}	8	0.567	12.2	1.2×10^{-3}	4.4×10^{-6}
8	0.580	12.5	3.0×10^{-4}	1.1×10^{-6}	9	0.624	13.4	1.3×10^{-3}	5.1×10^{-6}
9	0.637	13.7	1.7×10^{-4}	6.9×10^{-7}	10	0.681	14.6	1.3×10^{-3}	5.4×10^{-6}
10	0.695	14.9	1.8×10^{-6}	7.9×10^{-9}	11	0.740	15.9	1.2×10^{-3}	5.5×10^{-6}

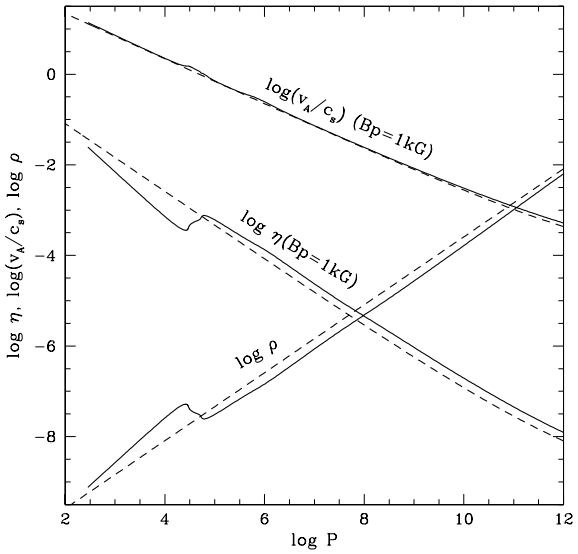

Figure 2. The ratio of the Alfvén speed to the sound speed (v_A/c_s), the quantity η, and the gas density in the stellar envelope. The Alfvén speed v_A and the quantity η are computed with a field strength of $B_p = 1$ kG. The full lines show the data for the 1.7-$M_\odot$ ZAMS model (Model 1), the dashed lines show data for the polytropic model. The sudden changes of quantities at $\log P \simeq 4.5$ arise from a density inversion.

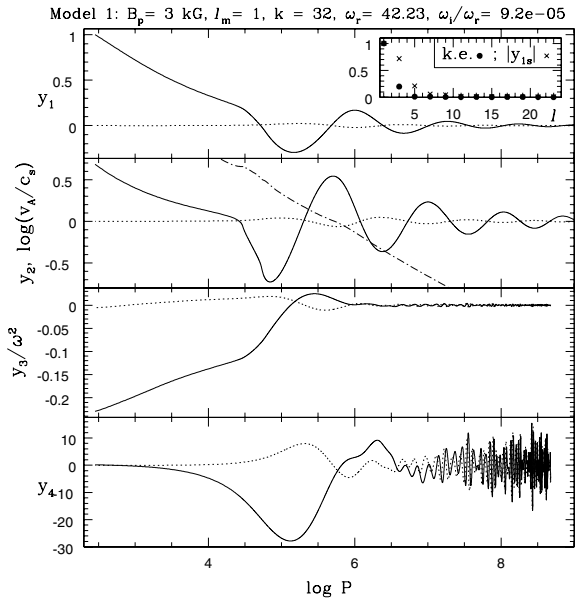

Figure 3. The eigenfunction of the 32nd-order p-mode with $\ell_m = 1$ at $B_p = 3.0$ kG. Although eight ℓ-components are sufficient for the convergence in frequency, twelve ℓ-components are included to obtain accurate eigenfunctions. Solid and dotted lines show the real and imaginary parts, respectively, for the $\ell = \ell_m$ components for y_1, y_2 and y_3, and for the $\ell = \ell_m + 1$ component for y_4. The lines for the variables y_3 and y_4 stop at $\log P = 8.68$ ($r/R = 0.95$), where the running wave inner boundary conditions are imposed. The dot-dashed line in the middle panel refers to $\log(v_A/c_s)$. The inset in the uppermost panel depicts the relative distribution of the kinetic energies among the various ℓ-components (filled circles) and the amplitude of y_1 (cross) at the outermost grid point.

than unity; the Alfvén speed, however, exceeds the sound speed above the photosphere for $B_p = 1$ kG. Hence, in roAp stars, the pulsational motion should be strongly affected by the magnetic field in the zone of spectral-line formation.

5 NUMERICAL RESULTS

To obtain the eigensolution of a pulsation mode at a chosen magnetic field strength, we performed computations with at least two choices of n_c (the number of ℓ-components); i.e. $n_c = n$ and $= n - 1$. We have adopted the result obtained with $n_c = n$ as a solution if the following two conditions are satisfied: (i) the kinetic energy in the last ℓ-component is less than half of the maximum value among the other ℓ-components, and (ii) the real part of the eigenfrequency differs by less than 0.1 per cent from that obtained with $n_c = n - 1$. Otherwise, we repeated the computations by increasing the value of n until the above two conditions were satisfied, or until n reached 12, the maximum number of ℓ-components we considered. If the above two requirements were not met even at $n_c = 12$, the result was discarded. In most cases we started with $n = 8$. Unless stated otherwise, we did not include the imaginary parts of the eigenfrequencies in checking the quality of the eigensolution. The differences in the imaginary parts between the results obtained with $n_c = n$ and with $n_c = n - 1$ are less than 20 per cent in most cases. However, when the magnetic damping rate is very large, the imaginary part could differ by as much as a factor of two.

In the following, we identify a mode by ℓ_m and k. The quantity ℓ_m refers to the ℓ-component of the expansion with largest kinetic-energy contribution, and k is the number of nodes in the real part of y_{1,ℓ_m}.

5.1 Eigenfunctions

Fig. 3 shows the real (solid lines) and the imaginary (dotted lines) parts of $y_{1,1}$, $y_{2,1}$, $y_{3,1}$ and $y_{4,2}$ for the 32nd-order $\ell_m = 1$ p-mode in the presence of a magnetic field of $B_p = 3$ kG. The dot-dashed line in the middle panel refers to the ratio of the Alfvén to the sound speed. Fig. 4 shows the eigensolution for the same p-mode but at a magnetic field strength of $B_p = 0.3$ kG.

The usual acoustic eigenfunctions $y_{1,1}$ and $y_{2,1}$ are hardly affected by the presence of a magnetic field, even in the layers where the Alfvén speed exceeds the sound speed. This property may indicate that the driving due to the κ-mechanism in the partial hydrogen ionization zone, which excites p-modes in the roAp period domain, is not drastically modified by the presence of a strong magnetic field. However, the superposition of the various ℓ-components might modify considerably the non-adiabatic property of the mode. Although it is beyond the scope of this paper, a quasi-adiabatic-type analysis would be a first step to examine the magnetic effect on the κ-mechanism, as indicated by the referee of this paper.

The horizontal component of the perturbation of the magnetic field, which is proportional to y_4, is small near the outer boundary where the source-free potential-field condition is imposed. A significant perturbation of the magnetic field starts in a layer where the Alfvén speed is comparable to the sound speed and propagates inward as a slow wave. The wavelength of the spatial oscillations is proportional to $\sqrt{\eta}/\omega$ (equation 16). Since η, which is proportional to the magnetic energy to the gas pressure, decreases with increasing the gas pressure (Fig. 2), the wavelength continues to decrease towards the stellar centre. The rapid spatial oscillations of the eigenfunction of y_3 are also due to the slow wave.

Slow waves will be completely dissipated before reaching the stellar centre (Roberts & Soward 1983) so that it is well justified to impose running-wave boundary conditions for y_4 and y_3 at a depth

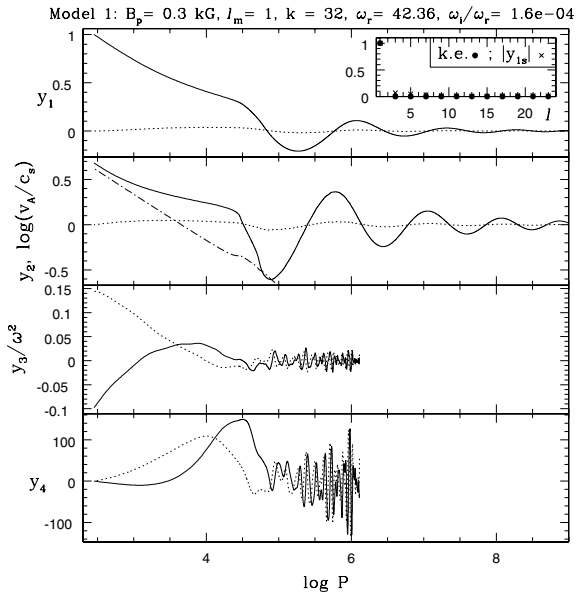

Figure 4. The same as Fig. 3 but for $B_{\rm p} = 0.3$ kG. In this case the running wave conditions for y_3 and y_4 are imposed at $r/R = 0.992$ ($\eta = 10^{-5}$).

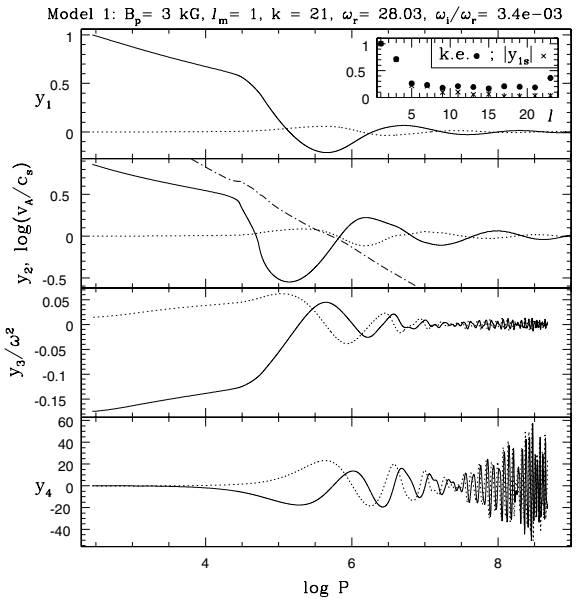

Figure 5. The same as Fig. 3 but for a lower-order mode with $k = 21$. The damping rate is much higher than the case of the $k = 32$ mode at the same value of $B_{\rm p}$. The kinetic energy is broadly distributed among ℓ-components.

$r = r_{\rm b}$, where the wavelength of slow waves is sufficiently small compared to the wavelength of acoustic waves, i.e. wavelengths of variations in y_1 and y_2. For the cases shown in Figs 3 and 4, $r_{\rm b} = 0.95R$ and $0.992R$, respectively. A shallower boundary such as in the latter case is necessary for a small value of $B_{\rm p}$ to avoid losing the accuracy of eigenfunctions with a given number of grid points of the model star.

The energy leak caused by slow waves damps even adiabatic pulsations and hence leads to complex eigenfrequencies and eigenfunctions. For the mode shown in Figs 3 and 4 the amplitude damping rate ($\omega_{\rm i}/\omega_{\rm r}$) is 9.2×10^{-5} at $B_{\rm p} = 3$ kG and 1.6×10^{-4} at $B_{\rm p} = 0.3$ kG. The strength of damping by slow waves does not change monotonically with the magnetic field strength. We will return to this point later.

The insets in the top panels of Figs 3 and 4 show the contributions of the various ℓ-components to the eigensolutions. The dots refer to the normalized kinetic energy contributions of the terms in the expansion. The smaller the contributions from higher ℓs are, the better the convergence is. The distribution in ℓ of the surface amplitudes of $y_{1\rm s}$ (y_1 at the outermost grid point) is shown as crosses in the insets. The contribution to the amplitude from components with $\ell \neq \ell_{\rm m}$ can be considerable even if the kinetic energy is well concentrated in the $\ell = \ell_{\rm m}$ component. This means that in general the latitudinal variation of the amplitude on the surface deviates considerably from the Legendre function $P_{\ell_{\rm m}}(\cos\theta)$, which agrees with the results of the previous investigations by Dziembowski & Goode (1996), Bigot et al. (2000) and Cunha & Gough (2000).

The quantity $y_3/\omega^2 = \xi_{\rm p}/r - y_2/\omega^2$ expresses the horizontal displacement caused by the perturbation of the magnetic field (see equation B3). Fig. 3 shows that y_3 has a large amplitude above the photosphere ($\log P = 4.42$), where the Alfvén velocity exceeds the sound velocity. The horizontal displacement around the surface can be as large as ~20 per cent of the radial displacement y_1, and is much larger than y_2/ω^2, the horizontal displacement expected in the absence of a magnetic field. We note that the comparatively large horizontal displacement might need to be accounted for in the interpretation of radial-velocity and line-profile variations.

Fig. 5 contains the same information as Fig. 3, but shows the 21st-order p-mode of $\ell_{\rm m} = 1$ at $B_{\rm p} = 3$ kG. The variations of y_1 and y_2 above the photosphere are appreciably less steep than those for the $k = 32$ mode in Fig. 3. The damping rate of the 21st p-mode at $B_{\rm p} = 3$ kG is $\omega_{\rm i}/\omega_{\rm r} \simeq 3.4 \times 10^{-3}$, which is much higher than what we found for the other two cases. The amplitude of slow-wave oscillations in y_4 increases rapidly inward, indicating a large leakage of pulsation energy. The inset in the top panel of Fig. 5 shows that the kinetic energy is distributed broadly among the ℓ-components. Accordingly, the convergence of the expansion is not very good in this case. Weak convergence occurs when the damping rates become very high, irrespective of the order of the mode.

5.2 Eigenfrequencies

This subsection describes magnetic effects on eigenfrequencies of p-modes of various orders at various field strengths. The presence of a magnetic field shifts the real part of the eigenfrequency, $\omega_{\rm r}$ (pulsation frequency); furthermore, it makes the imaginary part of the eigenfrequency, $\omega_{\rm i}$, positive (i.e. damps the pulsation). The amplitude damping time in seconds is given by $\sigma_{\rm i}^{-1}$.

5.2.1 High-order modes

We begin by discussing the sensitivity of the numerical results for eigenfrequencies to the position where the running wave conditions for y_3 and y_4 are imposed ($r = r_{\rm b}$). If $r_{\rm b}$ is too close to the outer boundary, the wavelengths of the slow waves are not short compared to those of the acoustic pulsation so that the short-wave approximation is not appropriate. On the other hand, if the boundary is located too deep, the wavelengths of the slow waves become too short to be spatially resolved by the grid points of the star model. Therefore, a compromise must be sought.

Fig. 6 compares eigenfrequencies of the 33rd p-mode of $\ell_{\rm m} = 1$ at various $B_{\rm p}$ obtained by imposing the running wave condition at $r_{\rm b} = 0.95R$ (filled circles) with those obtained by imposing it at $0.97R$

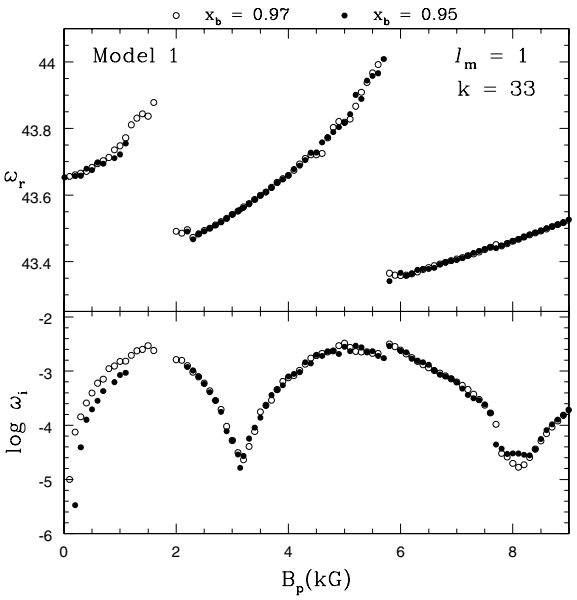

Figure 6. The eigenfrequency of the 33rd-order $\ell_{\rm m} = 1$ p-mode of Model 1 as a function of $B_{\rm p}$, the strength of the magnetic field at the poles on the stellar surface. The upper and lower panels show the real and imaginary parts of the eigenfrequency, respectively. To check the sensitivity of the results to the location of the inner boundary ($r = r_{\rm b}$) for y_3 and y_4, eigenfrequencies were computed with two different values of $r_{\rm b}$: $0.95R$ (filled circles) and $0.97R$ (open circles).

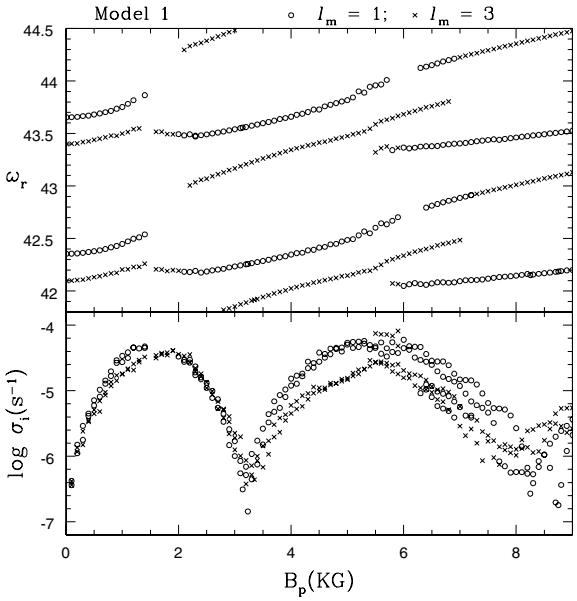

Figure 7. The real parts of the eigenfrequencies (upper panel) and the corresponding damping rates (lower panel) of some high-order p-modes with $\ell_{\rm m} = 1$ and 3 as a function of $B_{\rm p}$.

(open circles). The agreement between the two cases is generally very good, indicating that the running wave condition works well. For $B_{\rm p} \lesssim 1$ kG, $\omega_{\rm i}$ tends to be smaller for the case of $r_{\rm b} = 0.95R$ as compared to $r_{\rm b} = 0.97R$, which might be taken as a sign of insufficient spatial resolution in the former case.

In some $B_{\rm p}$ sections in Fig. 6 no eigenfrequency is plotted. This is due to the fact that our method sometimes fails to obtain an eigensolution which meets the accuracy requirements discussed at the beginning of Section 5. Such failures tend to occur when the damping rate of a mode is very high, i.e. when the kinetic energy is distributed over many ℓ-components.

Fig. 6 indicates that a shallower boundary works better around the first peak in the damping rate, while at higher $B_{\rm p}$ values the results are insensitive to the choice of $r_{\rm b}$. Taking into account the facts that a shallower boundary works better at small $B_{\rm p}$ values and that $v_{\rm A} \approx c_{\rm s}$ at $r/R \simeq 0.95$ for $B_{\rm p} = 10$ kG, we have adopted $r_{\rm b} = \max[r(\eta = 10^{-5}), 0.95R]$ as the canonical choice in our computations. That prescription for $r_{\rm b}$ leads to $r_{\rm b}/R = 0.976$ at $B_{\rm p} = 1$ kG and $r_{\rm b}/R = 0.95$ for $B_{\rm p} > 2.5$ kG.

The magnetic effect on the eigenfrequency of pulsation changes cyclically as the field strength increases. This property was first found by Cunha & Gough (2000) in the context of the roAp stars. The real parts of eigenfrequencies change rather abruptly at some values of $B_{\rm p}$, at which the imaginary parts go through a local maximum. The effect of a magnetic field on the oscillation frequencies does not depend significantly on the dominant spherical degree, $\ell_{\rm m}$. The real part of the eigenfrequency of a mode, $\omega_{\rm r}$, generally increases as the magnetic field gets stronger, except at distinct values of $B_{\rm p}$, where $\omega_{\rm r}$ decreases abruptly and the damping rate goes through a local maximum.

Fig. 7 shows frequency (upper panel) and damping rate (lower panel) of some odd modes with $\ell_{\rm m} = 1$ and 3. The eigensolutions at $B_{\rm p} = 0$ in this figure are classified as $(\ell, k) = (3, 31)$, $(1, 32)$, $(3, 32)$ and $(1, 33)$ in order of increasing frequencies. The damping rate, $\sigma_{\rm i}$, measures the amount of dissipation due to the magnetic slow waves. The frequencies and damping rates of the modes shown in Fig. 7 increase with $B_{\rm p}$ up to about 1.5 kG, at which the damping rate becomes a local maximum and the expansion of eigenfunctions starts to fail. At $B_{\rm p} \simeq 2$ kG it starts to converge again. However, the kinetic energy is still broadly distributed among the ℓ-components so that for $B_{\rm p} \simeq 1.5$–2 kG the mode along on an $\ell_{\rm m} = 1$ sequence becomes as an $\ell_{\rm m} = 3$ mode. In the range of 2 kG $< B_{\rm p} <$ 6 kG, the oscillation frequency increases gradually with $B_{\rm p}$, while the damping rate goes through a sharp minimum at about $B_{\rm p} \simeq 3.1$–3.3 kG. The diminishing of damping occurs when the slow waves are well trapped in the outer layers where the Alfvén speed exceeds the sound speed. We will return to this trapping concept later. There is another local maximum of the damping rate at $B_{\rm p} \sim 6$ kG, where the real part of the eigenfrequency makes a sudden decrease. As in the case of the low-$B_{\rm p}$ damping maximum, mode identification is ambiguous here because of the broad distribution of the kinetic energy among ℓ-components.

Fig. 8 is the same as Fig. 7 but for even modes with $\ell_{\rm m} =$ 0 and 2. This figure includes, in order of increasing frequencies, $(\ell, k) = (0, 30)$, $(2, 30)$, $(0, 31)$ and $(2, 31)$ at $B_{\rm p} = 0$. The magnetic effect on the even modes is more complex than that on odd modes. An $\ell_{\rm m} = 0$ mode sequence starting from $B_{\rm p} = 0$ terminates at $B_{\rm p} \sim 1.3$ kG where the damping rate is close to a local maximum. The sequence terminates because the convergence of the expansion into ℓ-components fails. Around the end of the sequence, the mode appears as an $\ell_{\rm m} = 2$ mode. On the other hand, a mode sequence starting as $\ell_{\rm m} = 2$ at $B_{\rm p} = 0$ has no convergence problem around the first damping-rate peak, although a large contribution from the $\ell = 0$ component sometimes shifts $\ell_{\rm m}$ to 0 there. (An $\ell_{\rm m} = 2$ mode whose kinetic energy in the $\ell = 0$ component exceeds 70 per cent of that in the $\ell = 2$ component is plotted with a filled square in Fig. 8.) The sequence is terminated at $B_{\rm p} \simeq 2.5$ kG because $\ell_{\rm m}$ shifts to 4 there.

The identification of the order of $\ell_{\rm m} = 0$ modes is somewhat ambiguous in the range of $B_{\rm p}$ between the first and the second

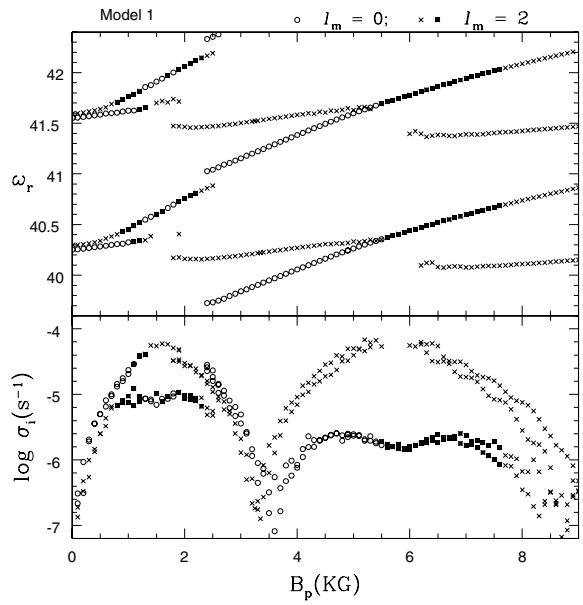

Figure 8. The same as Fig. 7 but for p-modes with $\ell_m = 0$ and 2. Two kinds of symbols are used for $\ell_m = 2$ modes; a filled square indicates a mode in which the $\ell = 0$ component has a kinetic energy more than 70 per cent of that of the $\ell = 2$ component.

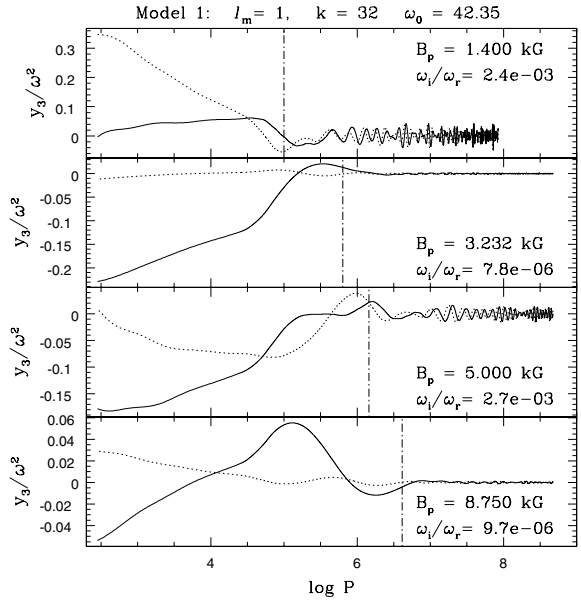

Figure 9. Radial variation of $y_{3,1}$ of the $(\ell_m, k) = (1, 32)$ mode with respect to log P for selected magnetic field strengths. Solid and dotted lines show the real and the imaginary parts, respectively. Vertical dash-dotted lines indicate the position where the sound speed is equal to the Alfvén speed. The second and the fourth panels depict modes close to the first and the second minima of the damping rate, respectively (cf. Fig. 7). Note that for the cases with small damping rates, y_3 is well trapped in the outer layers where the Alfvén speed exceeds the sound speed.

damping maxima (2.5 kG $\lesssim B_p \lesssim$ 5 kG in Fig. 8). The $\ell_m = 0$ mode having a frequency of $\omega_0 \simeq 41.55$ at $B_p \simeq 0$ kG, for example, is identified as $k = 31$ with 31 nodes in the real part of $y_{1,0}$. An $\ell_m = 0$ mode sequence starts at (ω_r, B_p) = (41.0, 2.4 kG). The starting position on the diagram would be consistent with the occurrence of a rapid frequency decrease, similar to other ℓ_m cases, around the local damping maximum, if the number of nodes of the mode were 31. However, the value of k for the branch starting at 2.4 kG is 30. The pulsation frequency of the mode of this branch increases up to $\sim\omega_0$ of the $k = 31$ mode before it changes, at $B_p \simeq 5.5$ kG, to an $\ell_m = 2$ sequence with a large contribution from the $\ell = 0$ component. Such a mismatch in the order k occurs for all the $\ell_m = 0$ modes with $k \geqslant 19$ ($\omega_0 \geqslant 26.16$). We also note that the damping rates of $\ell_m = 0$ modes and of $\ell_m = 2$ modes with a large contribution from the $\ell = 0$ component are significantly smaller than the 'proper' $\ell_m = 2$ modes in the range of 4 kG $\lesssim B_p \lesssim$ 8 kG.

The damping rates for odd and even modes have sharp minima occurring cyclically as a function of B_p. If a pulsation mode excited by the κ-mechanism happened to be close to a minimum in the damping rate due to slow-wave leakage, the mode would probably survive in the presence of a strong magnetic field. We note, however, that the eigenfunction of an $\ell_m = 0$ mode in the presence of a strong magnetic field is influenced so strongly by $\ell = 4$ and 6 components in the outer stellar layers that the appearance of the pulsation on the surface would be far from spherically symmetric (see Section 5.3 below).

5.2.2 Trapping of magnetic slow waves

The appearance of sharp minima in the damping rates of p-modes can be understood as a trapping of slow waves in the superficial layer where the Alfvén speed (v_A) exceeds the sound speed (c_s). Fig. 9 shows spatial variations of $y_{3,1}/\omega^2$, which represents the horizontal displacement caused by the perturbation of the magnetic field, in the outer envelope for the $(\ell_m, k) = (1, 32)$ mode at various field strengths B_p. The vertical dash-dotted lines indicate the position where $v_A = c_s$. The second and the fourth panels from the top are for $B = 3.232$ kG and 8.75 kG, respectively, at which the slow-wave damping of the pulsation diminishes significantly. The other panels show the cases with large damping. In the cases of diminished damping the eigenfunction $y_{3,1}$ is obviously well trapped in the superficial magnetic layer where $v_A > c_s$; the trapping reduces the inward leak of energy.

In the case of $B_p = 3.232$ kG, one node in $y_{3,1}$ exists in the magnetic layer. On the other hand, we find two nodes to exist in the case of $B_p = 8.75$ kG. Thus, if B_p is continuously increased for a given mode, the trapping occurs cyclically with the number of nodes of y_3 in the magnetic superficial layer increasing by one for each cycle. The same phenomenon occurs if we increase the order k at a fixed value of B_p. This explains the cyclic appearance of the minima in the damping rates as a function of B_p for a fixed k (Figs 7 and 8), and as a function of k for a fixed B_p (Cunha & Gough 2000).

A large damping rate, on the other hand, occurs if $y_{3,1}$ has an antinode around the position where $v_A \approx c_s$. Consequently, the rapid spatial oscillations of the eigenfunction have appreciable amplitudes in the deeper layers indicating a significant leak of energy. We note that the properties of magnetic slow waves described above are essentially the same as those discussed by Cally & Bogdan (1993) and Bogdan & Cally (1997) for oscillations of a plane-parallel polytrope permeated by a vertical magnetic field.

5.2.3 Similarity of the magnetic effects on different modes

Figs 10 and 11 display the real parts of the eigenfrequencies as a function of B_p for Model 1 (1.7-M$_\odot$ ZAMS model). Fig. 10 shows odd modes with $\ell_m = 1$ and 3, and Fig. 11 even modes with $\ell_m = 0$

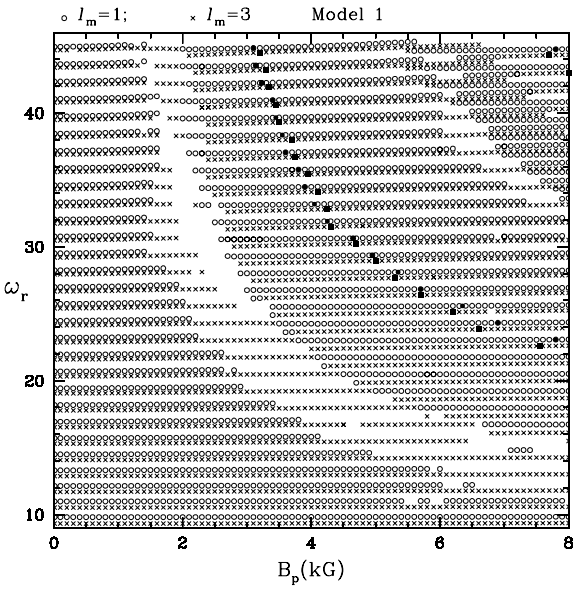

Figure 10. Real parts of the eigenfrequencies of odd modes of Model 1 plotted with respect to the magnetic field strength $B_{\rm p}$(kG). Open circles (crosses) stand for modes with $\ell_{\rm m} = 1$ ($\ell_{\rm m} = 3$). For $\ell_{\rm m} = 1$ ($\ell_{\rm m} = 3$), overtone orders from 6 (5) to 34 (33) are plotted. The expansion method fails to converge in the two narrow regions which run from upper left to lower right. Across these two narrow regions, the damping rates attain a local maximum and the frequency shift undergoes a sudden change. Filled symbols indicate the positions of local minima of the damping rates.

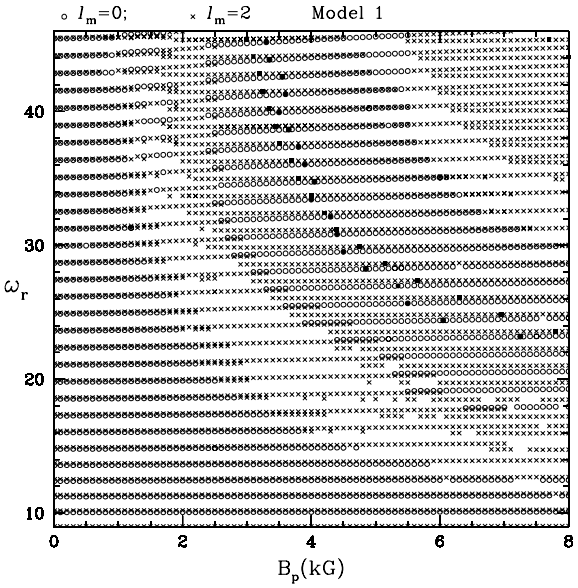

Figure 11. The same as Fig. 10 but for even modes. Open circles (crosses) stand for modes with $\ell_{\rm m} = 0$ ($\ell_{\rm m} = 2$). The diagram shows the range from the 6th to the 34th overtone for $\ell_{\rm m} = 0$ and 2.

and 2. Figs 10 and 11 are interlaced by two stripes within which no, or fewer, eigensolutions are plotted. In the two depopulated zones the damping rates of the pulsation attain a local maximum. At the same time, the expansion method has a convergence problem there; the numerical solutions tend to be sensitive to the number of ℓ-components included in the expansion as the kinetic energy of the modes is not confined to only a few ℓ-components.

The maximum-damping zones (zones of slow or even failing convergence) start to influence high-order modes first (i.e. at low magnetic field strengths) and propagate to lower overtones as the field strength increases. In the region in the lower-left to the first maximum-damping zone in the $B_{\rm p}$–$\omega_{\rm r}$ diagram, the magnetic effect at a given $B_{\rm p}$ is smaller for lower-order p-modes. This may be attributed, at least partially, to the fact that the pulsation-energy distribution of lower-order modes has more weight in deeper zones where the ratio of magnetic to gas pressure is small.

The loci of minimum damping in Figs 10 and 11 (indicated by filled symbols) run almost parallel to the maximum-damping zones. If a mode is excited by the classical κ-mechanism in a magnetic star, the mode probably survives if the magnetic damping rate is very small, i.e. if the mode is located around a filled symbol. Such optimal field strength for diminished damping is about 3 kG (and about 8 kG) for high-order modes, and it increases as the order of the mode decreases. This indicates that for an roAp star the magnetic field strength should be larger than a few kG, and furthermore, predicts that an roAp star having a stronger magnetic field tends to pulsate in relatively low-order modes.

The regularity seen in Figs 10 and 11 hints at the existence of a similarity relation which scales the magnetic effect on p-modes with different frequencies at various magnetic field strengths. The similarity parameter for the effect of a magnetic field on the pulsations of a polytrope is proportional to $\omega_0\ B_{\rm p}^{1/(n+1)}$ (Roberts & Soward 1983; Campbell & Papaloizou 1986; Cunha & Gough 2000), where n is the polytropic index, and ω_0 the pulsation frequency in the absence of a magnetic field. Since our 1.7-$M_\odot$ model structures deviate from polytropic structures, we have assumed the form of the similarity parameter as $f_\alpha \equiv \omega_0 B_{\rm p}^\alpha$, and searched for the best value of α. We have obtained $\alpha = 0.7$ as the best choice for intermediate-to-high overtone p-modes. This exponent corresponds to an effective polytropic index of 0.43. The small effective polytropic index must be attributed to the density inversion in the model structure. The effective polytropic index represents some average of the polytropic index in the outer layer where the magnetic effect is significant. Therefore, the effective polytropic index is expected to be lowered significantly by the existence of a density inversion as a density inversion corresponds to a negative polytropic index. We note also that a single value of α cannot cover the whole spectrum of p-modes because the effective polytropic index varies with pulsation frequency. Actually, we will find below that $\alpha = 0.35$ (corresponding to an effective polytropic index of ~ 1.9) works well for low-order p-modes.

Figs 12 and 13 show magnetic frequency shifts, $\Delta\omega = \omega(B_{\rm p}) - \omega_0$, with respect to $f_{0.7}$. The upper and lower panels are for the real and imaginary parts, respectively. Fig. 12 is for $\ell_{\rm m} = 1$ modes and Fig. 13 for $\ell_{\rm m} = 3$ modes. The big squares show the results of various orders of p-modes of Model 1 computed at $B_{\rm p} = 4.0$ kG. Small symbols represent the frequency shifts at various $B_{\rm p}$ for $\ell_{\rm m} = 1, k = 21, 31$ modes (Fig. 12) and $\ell_{\rm m} = 3, k = 20, 30$ modes (Fig. 13) of Model 1 and Model 2. There is some ambiguity in the mode identification around the second damping peak. As seen in Fig. 7, between the second and the third damping peak (the third peak is outside of the diagram) a $\ell_{\rm m} = 3$ mode sequence appears as a $\ell_{\rm m} = 1$ mode sequence close to the second peak ($6 \lesssim B_{\rm p}$(kG) $\lesssim 7$ in the diagram). Considering the $\ell_{\rm m} = 1$ branch as the extension of the $\ell_{\rm m} = 3$ sequence, we have plotted the frequency shifts for the whole sequence as a $\ell_{\rm m} = 3$ mode sequence in Fig. 13. This causes 'double values' in $\Delta\omega_{\rm r}$ in Fig. 13 in a range of $150 \lesssim f_{0.7} \lesssim 165$.

In each of Figs 12 and 13, all the selected data collapse reasonably well on to a common modulation curve for $\Delta\omega_{\rm r}$ and $\omega_{\rm i}$ as

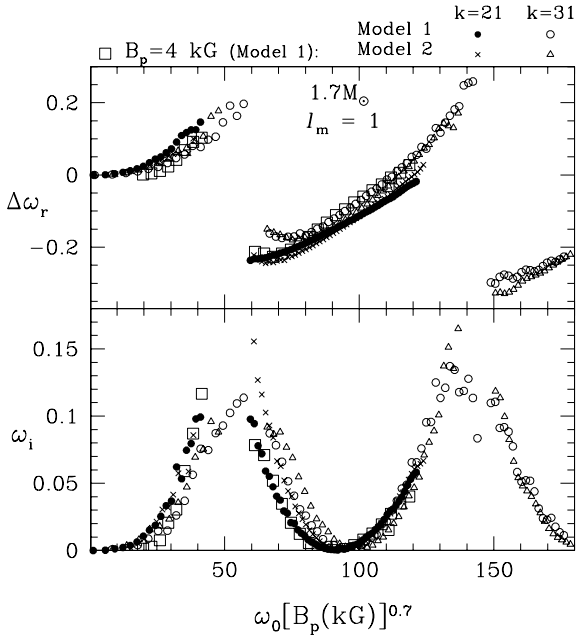

Figure 12. Frequency shift $\Delta\omega \equiv \omega(B_{\rm p}) - \omega_0$ versus $\omega_0[B_{\rm p}({\rm kG})]^{0.7}$ for $\ell_{\rm m} = 1$ modes of Model 1 and 2. The upper panel shows the real part $\Delta\omega_{\rm r}$, the lower panel the imaginary part $\omega_{\rm i} = \Delta\omega_{\rm i}$. Large squares indicate frequencies of various orders of p-modes at $B_{\rm p} = 4$ kG of Model 1. Filled circles depict the 21st ($\omega_0 = 28.26$), and open circles the 31st ($\omega_0 = 41.06$) overtones of Model 1. Crosses stand for the 21st, open triangles for 31st overtone p-modes of Model 2, all at various strengths of the magnetic field.

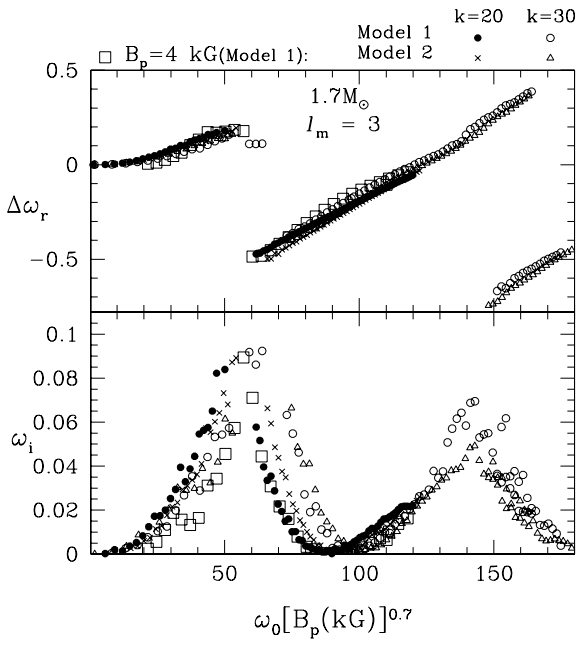

Figure 13. The same as Fig. 12 but for $\ell_m = 3$ and for the 20th ($\omega_0 = 27.95$ for Model 1) and the 30th ($\omega_0 = 40.79$ for Model 1) overtone p-modes.

a function of $f_{0.7}$, indicating that $f_{0.7}$ works well as a similarity parameter for the effect of a magnetic field on intermediate-to-high-order p-modes. The character of the modulations for $\ell_{\rm m} = 1$ modes is qualitatively the same as that for $\ell_{\rm m} = 3$ modes. Around $f_{0.7} = 50$ and 140, $\Delta\omega_{\rm r}$ varies abruptly after it grew smoothly upon increasing $f_{0.7}$. Simultaneously with the sharp $\Delta\omega_{\rm r}$ decline, $\omega_{\rm i}$ attains a local maximum. Such a maximum means that either for a given frequency the damping grows strongly at some magnetic field strength, or fixing a magnetic field strength, the damping gets strong for some radial orders. This phenomenon repeats itself; Figs 12 and 13 reveal two maxima in the damping rates (see also Fig. 10).

The magnitudes of the jump in $\Delta\omega_{\rm r}$ for $\ell_{\rm m} = 1$ modes (Fig. 12) are $\sim$0.4 and $\sim$0.55 at the first and second peaks of $\omega_{\rm i}$, respectively. For $\ell_{\rm m} = 3$ modes (Fig. 13), the corresponding quantities are $\sim$0.7 and $\sim$ 0.9. The magnitudes of the jump for $\ell_{\rm m} = 3$ modes are about 50 per cent larger than for $\ell_{\rm m} = 1$ modes. This is consistent with the results of Cunha & Gough (2000), although their values tend to be about 30 per cent larger than our results; see also Section 6.1.1 below. The peaks of the damping rates are not well resolved numerically. As mentioned before, around the damping maxima, the expansion method encounters convergence problems with the pulsation energy being distributed over many different ℓ-components, and the computations frequently fail to meet our convergence criteria. Nevertheless, Figs 12 and 13 seem to indicate that the peak of $\ell_{\rm m} = 1$ modes is higher than that of $\ell_{\rm m} = 3$ modes, which agrees qualitatively with fig. 3 in Cunha & Gough (2000).

The magnetic damping rates are very small for $f_{0.7} \simeq 90$ and 180, for which slow waves are trapped in the outer magnetic layers. These two values of $f_{0.7}$ correspond to the two sequences of filled symbols in Fig. 10. (The second one is barely seen in the upper right corner.) These circumstances offer 'frequency windows' where p-modes excited by the κ-mechanism can survive even in the presence of a strong magnetic field.

We have not produced f_α–$\Delta\omega$ diagrams for even modes because mode identification for even modes is too ambiguous, as discussed above. Comparing Fig. 8 with Fig. 7, however, we expect that the values of $f_{0.7}$ for diminished damping or maximum damping for even modes are similar to the corresponding values for odd modes.

5.2.4 Damping rates of low-order modes

The damping rates of low-order p-modes in the lower-left region in Figs 10 and 11 (bounded by the zone of the first damping peak) increase as $B_{\rm p}$ increases. It is interesting to examine whether damping by magnetic slow waves becomes sufficiently strong, at reasonable values of $B_{\rm p}$, to suppress low-order (i.e. δ Sct-type) pulsations which are excited by the κ-mechanism operating in the second helium ionization zone. In the absence of a magnetic field, several low-order modes are overstable in our 1.7-$M_\odot$ models as shown in Table 2. Since the κ-mechanism excitation is stronger in our evolved model (Model 2) than in the ZAMS model (Model 1), we compare the growth rates with the magnetic damping rates for low-order pulsations of Model 2.

Fig. 14 shows amplitude damping rates $\sigma_{\rm i}$ versus $f_{0.35}$ for some of the low-order modes of Model 2. (The exponent 0.35 to $B_{\rm p}$ corresponds to an effective polytropic index of $\simeq$1.86.) For the $k = 2$ modes, the running wave condition is imposed at $r/R = 0.90$, which is deeper than that for the modes with $k > 2$. A deeper boundary is necessary for slow waves to have short enough spatial wavelengths, which are proportional to $\sqrt{\eta}/\omega$ (equation 16). Obtained damping rates sometimes happen to be sensitive to the number of ℓ-components included, especially for very low damping rates ($\sigma_{\rm i} \lesssim 10^{-8}$ s^{-1}). To avoid the uncertainty, we have plotted in Fig. 14 only those damping rates whose numerical calculation including twelve ℓ-components agrees with that including eleven ℓ-components within 30 per cent.

Although there is considerable scatter, which comes from the inaccuracy of our numerical approach, the damping rates of

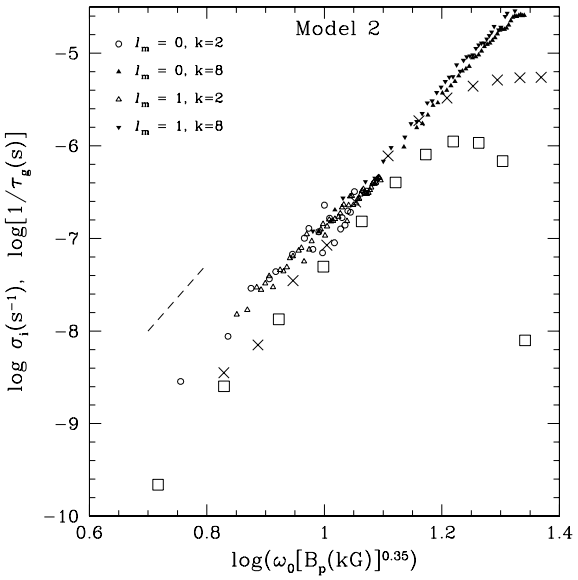

Figure 14. Amplitude damping rate due to energy drainage by magnetic slow waves versus the parameter $\omega_0 B_{\rm p}^{0.35}$ for various low-overtone modes of Model 2. Large squares ($\ell = 0$) and crosses ($\ell = 1$) indicate growth rates of low-frequency modes of Model 2 excited by the κ-mechanism in the absence of a magnetic field; to plot the growth rates in this diagram, we have arbitrarily chosen $B_{\rm p} = 3$ kG. The dashed line shows the slope derived from the theory developed by Roberts & Soward (1983).

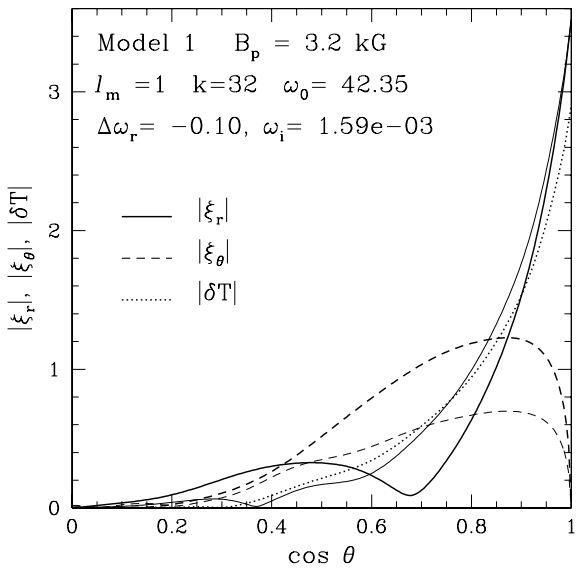

Figure 15. The modulus of the latitudinal amplitude distribution of the $k = 32$, $\ell_{\rm m} = 1$ mode of Model 1 in the presence of a magnetic field of $B_{\rm p} = 3.2$ kG. The full line stands for the radial component, ξ_r; the dashed line traces the horizontal component, ξ_θ, of the displacement. Thick and thin lines refer to the photosphere and the outer boundary (at $\tau = 0.002$), respectively. The dotted line shows the latitudinal run of the temperature perturbation in the photosphere. The quantity ω_0 is the normalized frequency of the mode in the non-magnetic state, and $\Delta\omega_{\rm r}$ is defined as $\omega_{\rm r}(B_{\rm p}) - \omega_0$.

low-overtone modes can be approximated by a monotonically increasing function of $f_{0.35}$ irrespective of $\ell_{\rm m}$ and of the order of modes. This relation between $\sigma_{\rm i}$ and $f_{0.35}$ is consistent with a relation derived from the results of Roberts & Soward (1983). According to their analysis, the damping rate of pulsation in the presence of a weak magnetic field should be proportional to $h^{(n+3)/(n+2)}$ with $h \propto B^2{}_z \omega^{2(n+1)}$, where B_z is the unperturbed vertical magnetic field and n the polytropic index. If we regard B_z as $B_{\rm p}$ and adopt $n = 1.86$, the above relation is converted to the relation that the damping rate is proportional to $(f_{0.35})^{7.2}$. This relation is shown by a dashed line in Fig. 14. The slope of the dashed line agrees with the slope of the numerical results, indicating that our results of the damping rates for low-order modes are consistent with the analysis by Roberts & Soward (1983).

We compare the $f_{0.35}$–$\sigma_{\rm i}$ relation with the growth rate of the δ Sct-type pulsations due to the κ-mechanism as given in Table 2. To plot the growth rates in Fig. 14, we must choose some value of $B_{\rm p}$. Adopting arbitrarily a field strength of $B_{\rm p} = 3$ kG, the growth rates are plotted as big open squares for $\ell = 0$ and as big crosses for $\ell = 1$ in Fig. 14. Needless to say, the big squares and the big crosses shift to the right if a larger value of $B_{\rm p}$ is chosen. We can say that if the growth rate of a mode is located below the $f_{0.35}$–$\sigma_{\rm i}$ relation of magnetic damping in Fig. 14, the magnetic damping exceeds the κ-mechanism driving and hence inhibits the amplitude of the mode to grow. Fig. 14 suggests that for $B_{\rm p} > 3$ kG, all the δ Sct-type pulsations, which are potentially excited by the κ-mechanism, are stabilized due to the presence of magnetic slow waves. We also note that the minimum field strength necessary to suppress the low-order p-modes is comparable to the lower limit of the field strength to have diminished damping rates for high-order p-modes (Fig. 10). Therefore, if we assume that an roAp star pulsates in high-order modes whose magnetic damping rates are very small, the lack of the δ Sct-type pulsation can be readily explained.

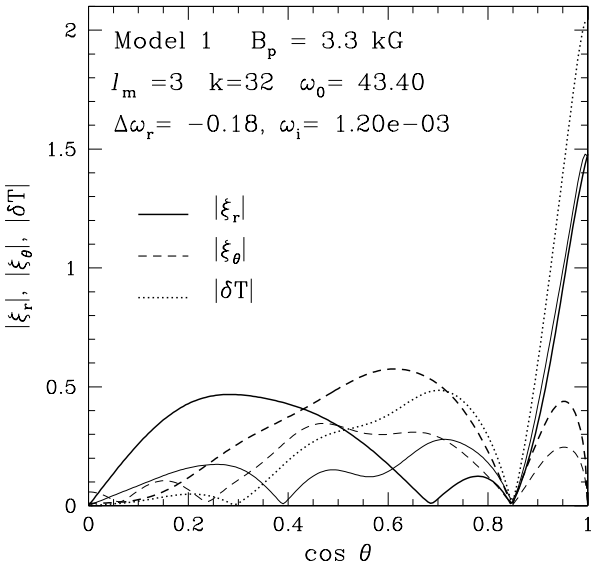

Figure 16. The same as Fig. 15 but for the $k = 32$, $\ell_{\rm m} = 3$ mode in the presence of a magnetic field of $B_{\rm p} = 3.3$ kG.

Although gravitational settling of helium was put forth as the cause of the lack of the δ Sct-type pulsation in roAp stars (e.g. Gautschy et al. 1998; Kurtz 2000), our results indicate that the damping by magnetic slow waves may be an important aspect in this phenomenon.

5.3 Latitudinal amplitude variation on the stellar surface

The latitudinal variation of the pulsation amplitude on the stellar surface is affected significantly by the presence of a magnetic field. Figs 15–18 show the latitudinal variation of the amplitudes of

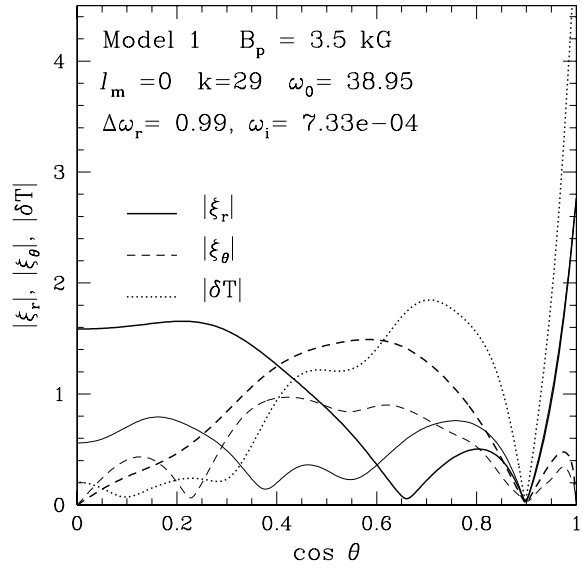

Figure 17. The same as Fig. 15 but for the $k = 29$, $\ell_m = 0$ mode in the presence of a magnetic field of $B_p = 3.5$ kG.

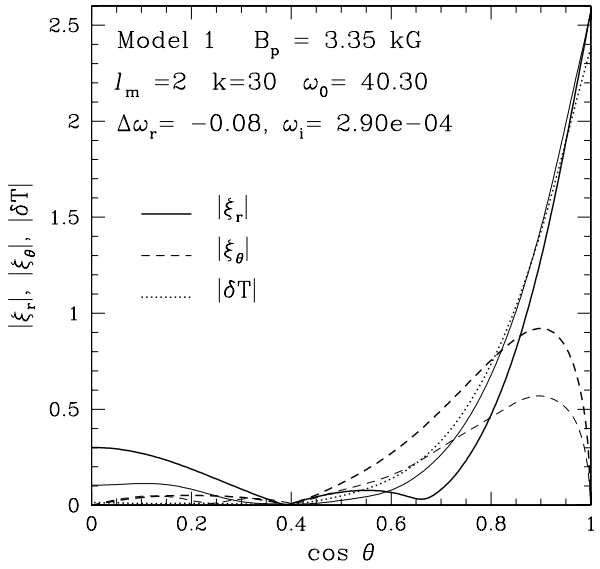

Figure 18. The same as Fig. 15 but for the $k = 30$, $\ell_m = 2$ mode in the presence of a magnetic field of $B_p = 3.35$ kG.

radial (solid lines) and horizontal (dashed lines) displacements and of temperature variation (dotted lines) of high-order modes in the photosphere (thick lines) and at the outer boundary at $\tau = 0.002$ (thin lines). The modes shown in these figures are some of those which appear in Figs 7 and 8 around the local minima of slow-wave damping so that they are expected to survive if they are excited by the κ-mechanism. Obviously, the latitudinal variation of pulsation amplitude cannot be represented by a single Legendre function.

Fig. 15 shows the 32nd $\ell_m = 1$ mode in the presence of a magnetic field of $B_p = 3.2$ kG. The temperature perturbation and radial displacements are more strongly concentrated at the magnetic polar regions than the $\cos\theta$ dependence expected for the mode in the absence of the magnetic effect. Such a strong concentration of the pulsation amplitude towards the magnetic axis is consistent with the recent observational results indicating that the amplitude of radial velocity variations in roAp stars is largest in the spectral lines of rare-earth elements which are overabundant in the magnetic polar regions (e.g. Malanushenko, Savanov & Ryabchikova 1998; Kochukhov & Ryabchikova 2001a,b; Balona & Zima 2002).

Non-radial oscillations of high-order, low-degree p-modes are nearly radial in the absence of a magnetic field. Fig. 15, on the other hand, demonstrates that the horizontal displacement is comparable to the radial displacement in the photosphere and above in the presence of a strong magnetic field. This figure shows also that the relative importance of the horizontal displacement is larger in the photosphere than at the outer boundary ($\tau = 0.002$). This is attributed to the fact that the radial displacement (being proportional to y_1) changes rapidly with depth in the case of a high-order p-mode, as can be seen in Fig. 3.

Fig. 16 is the same as Fig. 15 but for an $\ell_m = 3$ mode in the presence of a magnetic field of $B_p = 3.3$ kG. In this case the amplitude confinement to the polar regions is not as strong as in the case of $\ell_m = 1$ shown in Fig. 15. Even if this mode is excited, the light variation is expected to be small due to cancellation effects of the polar and the intermediate-latitude region bounded by a nodal line at $\cos\theta \simeq 0.85$. The radial-velocity variation, however, could be observable if it is observed in spectral lines of elements which are overabundant at the magnetic poles.

Fig. 17 shows the amplitude distribution on the surface of an $\ell_m = 0$ mode. The amplitude of the mode is very far from spherical symmetry. This is brought about by the large contributions from $\ell = 4$ and 6 components near the surface, although the kinetic energy of the mode is dominated by the $\ell = 0$ component. The large positive value of $\Delta\omega_r$ obtained for this mode comes from the ambiguity in the mode identification with respect to the number of radial nodes, k, as discussed in Section 5.2.1. If we compare the frequency of the mode with ω_0 of $k = 30$, rather than with that of $k = 29$, we obtain $\Delta\omega_r = -0.31$, which is comparable to other cases.

Fig. 18 shows the amplitude distribution on the surface for the 30th-order $\ell_m = 2$ mode with a magnetic field of $B_p = 3.35$ kG. The amplitude of this mode is well confined to the magnetic polar regions just like for the $\ell_m = 1$ mode shown in Fig. 15. However, since ξ_r and δT of an $\ell_m = 2$ mode are symmetric between the 'northern' and the 'southern' hemisphere, such a mode should show amplitude and phase modulations with the stellar rotation phase quite distinct from those of an $\ell_m = 1$ mode (see below for the amplitude modulation). We also note that the 'visibility' of the mode is increased by the existence of the magnetic field, because the amplitude of temperature variation near the equator, whose phase is opposite to that in the polar regions, is considerably reduced.

Before closing the discussion on the latitudinal amplitude variation, we have to caution that non-adiabaticity can modify eigenfunctions considerably near the surface. Furthermore, the non-adiabatic calculations without a magnetic field presented by Gautschy et al. (1998) hinted at a very superficial node, at about $\log P \simeq 2$, in a model with temperature inversion. Since the magnetic influence is strong close to the surface, non-adiabatic calculations including the effect of the magnetic field would be necessary to make detailed comparisons of theoretical predictions with observed radial-velocity variations.

5.4 Amplitude modulation

The amplitude of the light variation of an roAp star modulates as a function of the stellar rotation phase (Kurtz 1982). This phenomenon is interpreted as an axisymmetric mode whose axis aligns with the

magnetic axis rotating about the rotation axis (the oblique pulsator model; Kurtz 1982). The oblique pulsator model was generalized by Kurtz & Shibahashi (1986) including additional components of $Y_\ell^0(\theta, \phi)$. Since the pulsation pattern on the surface is significantly distorted from the one represented by a single spherical harmonic in the presence of a strong magnetic field as shown, for example, in Fig. 15, it is interesting to see how much the modulation curve is affected by the presence of a strong magnetic field.

In the adiabatic approximation, the Lagrangian temperature perturbation, δT, is proportional to the Lagrangian pressure perturbation. Therefore, δT of a pulsation mode can be represented by using the eigenfunction obtained by our numerical analysis as

$$\delta T(\theta, \phi, t) \propto \mathrm{e}^{\mathrm{i}\sigma t} \sum_{j=1}^{n_\mathrm{c}} (y_{2,\ell} - y_{1,\ell}) Y_\ell^0(\theta, \phi), \tag{20}$$

where n_c is the number of ℓ-components included, ℓ is a function of j defined by equations (13) and (14) for odd and even modes, respectively, and (θ, ϕ) are polar angles measured with respect to the magnetic axis. We assume that luminosity variation is due only to changes in temperature. Following the procedure described in, e.g. Unno et al. (1989), we can convert the coordinates associated with the magnetic axis into those associated with the line of sight. Then, we obtain an expression for the luminosity variation in the observer's frame:

$$\Delta L(t) \propto \mathrm{e}^{\mathrm{i}\sigma t} \sum_{j=1}^{n_\mathrm{c}} N_{\ell_j} (y_{2,\ell} - y_{1,\ell}) \sum_{m'=-\ell}^{\ell} d^{(\ell)}_{m'0}(\beta) d^{(\ell)}_{0m'}(\hat{\imath}) \mathrm{e}^{-\mathrm{i}m'\Omega t}, \tag{21}$$

where $\hat{\imath}$ is the inclination of the rotation axis to the line of sight, β the angle between the rotation and the magnetic axis, and m' the azimuthal order with respect to the rotation axis. The matrix $d^{(\ell)}{}_{m'_m}$ gives a relation between spherical harmonics associated with different axes of polar angles as

$$Y_\ell^m(\theta, \phi) = \sum_{m'=-\ell}^{\ell} Y_\ell^{m'}(\theta_\mathrm{R}, \phi_\mathrm{R})\, d^{(\ell)}_{m'm}(\beta), \tag{22}$$

where $(\theta_\mathrm{R}, \phi_\mathrm{R})$ are polar angles measured with respect to the rotation axis. The coefficients of the matrix can be calculated by using the Wigner formula (e.g. Messiah 1961). The effect of the amplitude integration over the visible stellar disc is included in N_ℓ which is defined as

$$N_\ell = \sqrt{2\ell + 1} \int_0^1 P_\ell(z)(1 - \mu + \mu z) z \, \mathrm{d}z, \tag{23}$$

where μ is the limb-darkening coefficient, and $z \equiv \cos\theta_\mathrm{L}$ with θ_L being the angle with respect to the line of sight. From equation (21), we obtain the amplitude modulation, $A(\Phi)$, with respect to the rotation phase Φ ($=\Omega t$) as

$$A(\Phi) \propto \left| \sum_{j=1}^{n_\mathrm{c}} N_\ell (y_{2,\ell} - y_{1,\ell}) \sum_{m'=-\ell}^{\ell} d^{(\ell)}_{m'0}(\beta) d^{(\ell)}_{0m'}(\hat{\imath}) \mathrm{e}^{-\mathrm{i}m'\Phi} \right|. \tag{24}$$

Equation (21) indicates that each m'-component should be observed with the pulsation frequency $\sigma - m'\Omega$, i.e. a single oblique pulsation mode shows multiple frequencies in the observer's frame. This corresponds to the rotational frequency splitting often observed in roAp stars (e.g. Kurtz 1990). (Since the effect of rotation is neglected in our analysis, no Coriolis term appears.) The pulsation amplitude, $A_{m'}$, of each m'-component can be obtained from equation (21), by exchanging the order of the summations, as

$$A_{m'} \propto \left| \sum_{\ell \geqslant |m'|} N_\ell (y_{2,\ell} - y_{1,\ell})\, d^{(\ell)}_{m'0}(\beta)\, d^{(\ell)}_{0m'}(\hat{\imath}) \right|. \tag{25}$$

Although there is an infinite number ($4n_\mathrm{c} - 1$ in the truncated system) of m'-components, only a few components with small values of $|m'|$ have appreciable amplitude due to cancellation on the stellar disc.

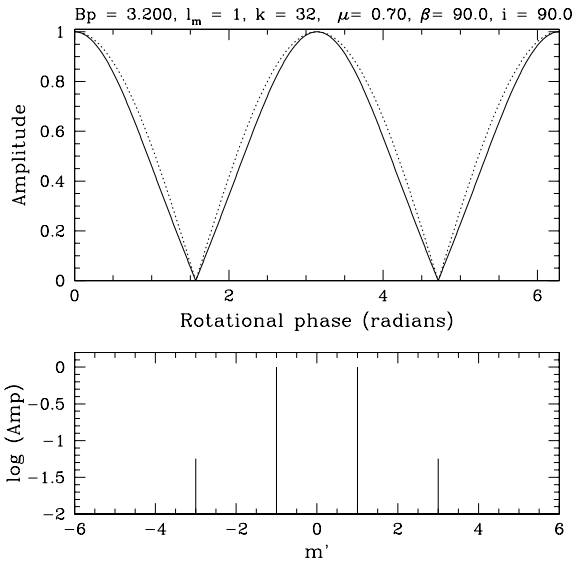

Figure 19. The amplitude modulation curve (upper panel) and corresponding amplitude spectra expected for a p-mode of $(\ell_\mathrm{m}, k) = (1, 32)$ in the presence of a magnetic field of $B_\mathrm{p} = 3.2$ kG. The inclination of the rotation axis, $\hat{\imath}$, and the magnetic obliquity, β are chosen as $(\beta, \hat{\imath}) = (90^\circ, 90^\circ)$. The limb-darkening is expressed as $(1 - \mu + \mu \cos\theta_\mathrm{L})$ with $\mu = 0.7$. The dotted line shows the amplitude modulation curve expected when the effect of the magnetic field is neglected; i.e. the pulsation pattern is given by the Legendre function $P_1(\cos\theta)$. The ordinate of the lower panel is the logarithm of the amplitude of each component, and the abscissa the azimuthal order with respect to the rotation axis.

Figs 19–22 show examples of the amplitude modulations and corresponding amplitude spectra obtained from equations (24) and (25), respectively, for the mode $(\ell_\mathrm{m}, k) = (1, 32)$ at $B_\mathrm{p} = 3.2$ kG with various $(\hat{\imath}, \beta)$. The limb-darkening coefficient is fixed as $\mu = 0.7$; the results are insensitive to the value of μ. Fig. 19 is for the case with $(\hat{\imath}, \beta) = (90^\circ, 90^\circ)$. The solid and dotted lines in the upper panel are derived from the eigenfunctions with and without magnetic effect, respectively. Although the magnetic effect on the amplitude distribution on the stellar surface is considerable (see Fig. 15), the effect on the amplitude modulation curve is very small. This comes from the fact that the surface integral of a brightness perturbation proportional to $P_\ell(\cos\theta)$ over a uniform-brightness disk cancels out for odd values of ℓ, except for $\ell = 1$; in other words, $\int_0^1 P_\ell(z) z \, \mathrm{d}z = 0$ in equation (23) for odd ℓ except for $\ell = 1$. Therefore, the effect of the deviation from the $P_1(\cos\theta)$ dependence appears in the amplitude modulation only through coupling with the limb-darkening of the stellar disc.

The amplitude spectrum derived from equation (25) is symmetric with respect to the sign of m' (azimuthal order with respect to the rotation axis) because we have neglected the effect of rotation on the eigenfunctions. The Coriolis force causes a small asymmetry between prograde and retrograde components (e.g. Shibahashi & Takata 1993; Bigot & Dziembowski 2002).

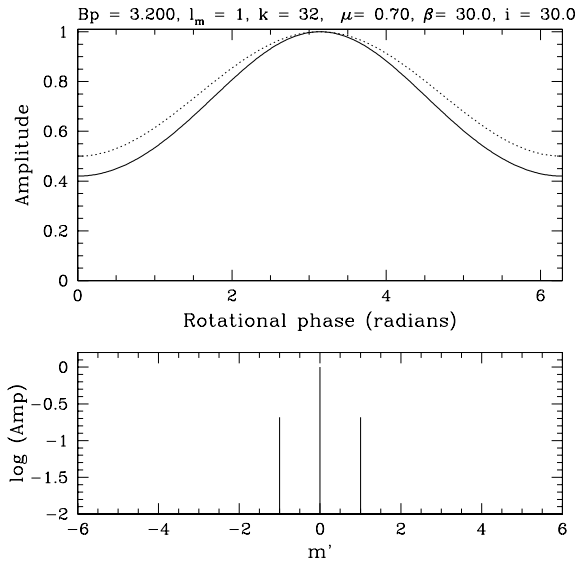

Figure 20. The same as Fig. 19 but for $(\beta, \hat{\imath}) = (30^\circ, 30^\circ)$.

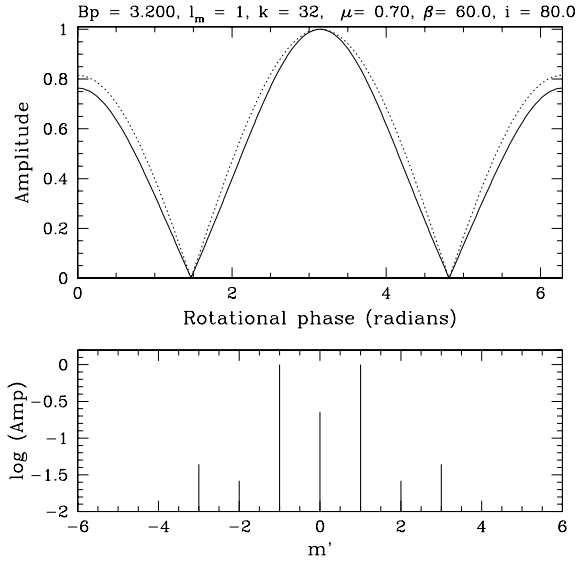

Figure 21. The same as Fig. 19 but for $(\beta, \hat{\imath}) = (60^\circ, 80^\circ)$.

The amplitudes for $|m'| \geqslant 2$ can be non-vanishing because the distorted eigenfunction is represented by a sum of the components of $\ell \geqslant 3$ in addition to the component of $\ell = 1$. If either β or $\hat{\imath}$ is 90°, the amplitude modulation has two peaks of equal height during one stellar rotation, and the amplitudes for the even $|m'|$-components vanish due to cancellation. The amplitudes for the odd m'-components except for $|m'| \leqslant 3$ are too small to be seen in Fig. 19.

Fig. 20 shows the case of $(\beta, \hat{\imath}) = (30^\circ, 30^\circ)$, an example of the circumpolar cases with $\beta + \hat{\imath} \leqslant 90^\circ$, in which only one maximum appears in the amplitude modulation curve for a period of rotation. The magnetic effect on the amplitude modulation curve in this case is slightly more visible than in the case of Fig. 19; the magnetic field makes the peak slightly narrower. In the amplitude spectrum, on the other hand, the amplitudes for $|m'| \geqslant 2$ components are too small compared to that of the $m' = 0$ component to appear in this figure.

Fig. 21 shows a case of $(\beta, \hat{\imath}) = (60^\circ, 80^\circ)$, in which the theoretical amplitude modulation curve is comparable to the observed one for HR 3831 (Kurtz et al. 1997). The similarity in the amplitude modulation is consistent with the fact that the ratio $A_0/A_{\pm1}$ is similar to the observed one. The amplitudes of the $|m'| = 2$ and 3 components ($A_{\pm2}/A_{\pm1} = 0.026$, $A_{\pm3}/A_{\pm1} = 0.044$) are, however, smaller than the observed ones [$(A_{-2} + A_{+2})/(A_{-1} + A_{+1}) = 0.070$, $(A_{-3} + A_{+3})/(A_{-1} + A_{+1}) = 0.087$]. If we adopt $(\beta, \hat{\imath}) = (33^\circ, 85^\circ)$ as in Shibahashi & Takata (1993) for HR 3831, we have smaller amplitudes for $|m'| = 2$ and 3 components, although the ratio $A_0/A_{\pm1}$ remains similar. We note here that the angles $(\beta, \hat{\imath}) = (8^\circ, 90^\circ)$ determined by Bagnulo, Landolfi & Landi Degl'Innocenti (1999) for HR 3831 yield amplitude modulation and an amplitude spectrum inconsistent with the observed ones as long as the pulsation axis is assumed to be close to the magnetic axis (cf. Bigot & Dziembowski 2002).

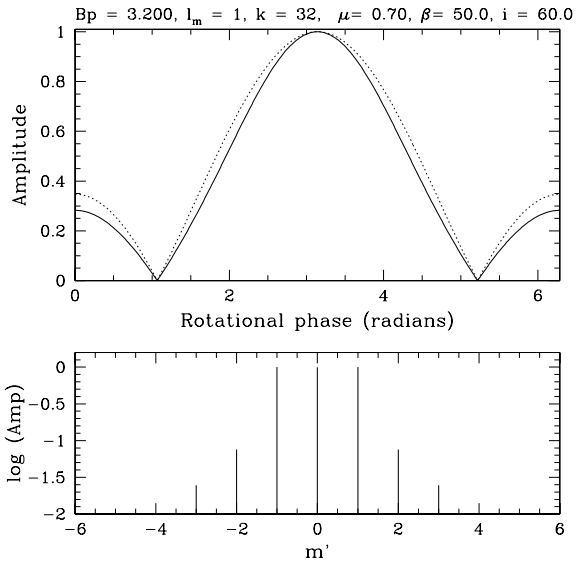

Figure 22. The same as Fig. 19 but for $(\beta, \hat{\imath}) = (50^\circ, 60^\circ)$.

Fig. 22 shows the amplitude modulation and corresponding amplitude spectrum for $(\beta, \hat{\imath}) = (50^\circ, 60^\circ)$. The amplitude modulation curve is comparable to the observed one for HD 6532 (Kurtz et al. 1996). However, the predicted amplitude ratio $A_{\pm2}/A_0 = 0.076$ is again smaller than the observed one, $0.5(A_{-2} + A_2)/A_0 = 0.20$.

The disagreements between the theoretical and observed values for $A_{\pm2}$ and $A_{\pm3}$ in the above two cases may be explained by non-adiabatic effects, or by the effect of a quadrupole component as discussed by Takata & Shibahashi (1995). More work is needed to make a detailed comparison between theory and observation.

Figs 23 and 24 contain the same information as Fig. 19 but for an even mode of $(\ell_m, k) = (2, 30)$ at $B_p = 3.35$ kG, whose amplitude variation on the surface is shown in Fig. 18. Two cases for the inclinations $(\beta, \hat{\imath}) = (90^\circ, 90^\circ)$ (Fig. 23) and $(30^\circ, 30^\circ)$ (Fig. 24) are shown. For an even mode the magnetic effect on the amplitude modulation is much larger than that for an odd mode. This comes from the property of the Legendre function; since $\int_0^1 z P_\ell(z)\,\mathrm{d}z \neq 0$ for even ℓ in equation (23), a large amplitude of the $\ell = 4$ component modifies considerably the amplitude modulation as well as the latitudinal amplitude variation on the surface. The secondary peaks in the amplitude modulation in the absence of a magnetic field (dotted line) is produced by the pulsation amplitude near the equator ($|P_2(\cos\theta)|$ with $\theta \sim \pi/2$). Since the magnetic effect significantly reduces the amplitude at the equator (see Fig. 18), the secondary peak is completely suppressed in Figs 23 and 24. As is

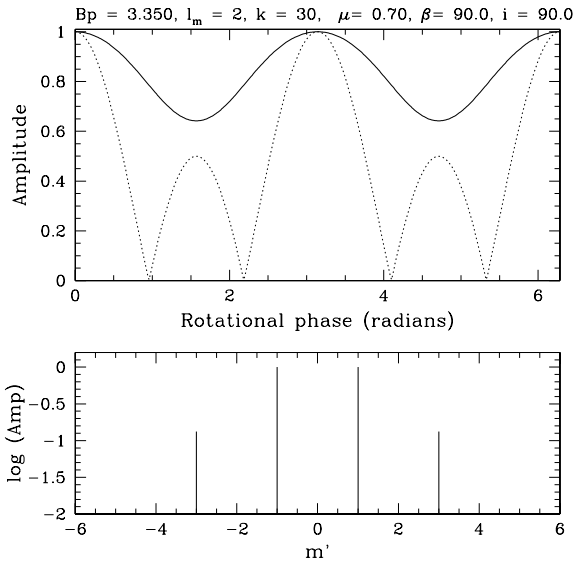

Figure 23. The same as Fig. 19 but for the even mode $(\ell_{\rm m}, k) = (2, 30)$ at $B_{\rm p} = 3.35$ kG for $(\beta, i) = (90^\circ, 90^\circ)$.

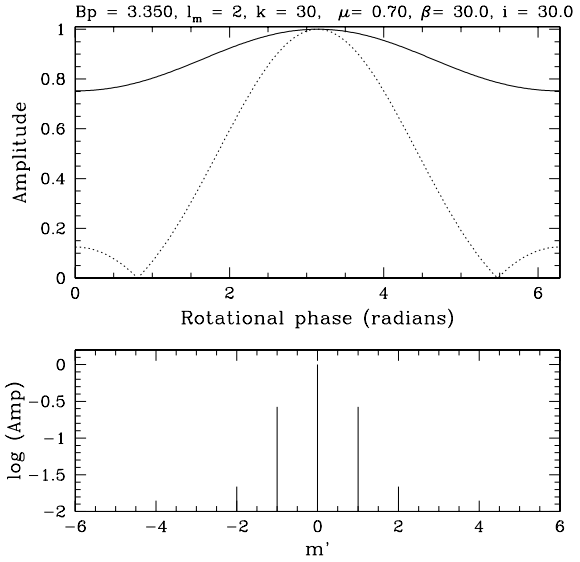

Figure 24. The same as Fig. 23 but for $(\beta, i) = (30^\circ, 30^\circ)$.

obvious from these figures, the magnetic effect reduces considerably the amplitude modulation of even modes by raising the minimum amplitude.

6 DISCUSSION

6.1 Comparison with previous results

6.1.1 Polytropic model

Using a variational principle, Cunha & Gough (2000) investigated the effect of a dipole magnetic field on high-order p-modes of an $n = 3$ polytropic model of 2 $M_\odot$ with a radius of 2 $R_\odot$. To check our method, we have applied our expansion analysis to the same kind of polytropic model. Our results for high-order p-modes with $\ell_{\rm m} \leqslant 3$ for the polytrope are shown in Fig. 25, where cyclic frequencies in physical units are plotted to make comparison with the results of Cunha & Gough (2000) easy. Mode sequences in these figures are terminated when the expansion into spherical harmonics fails or if $\ell_{\rm m}$ shifts to a value larger than 3. In Fig. 25 the mode order at $B_{\rm p} = 0$ is 29th for $\ell_{\rm m} = 0$, 2, 3, and 30th order for $\ell_{\rm m} = 1$. The $\ell_{\rm m} = 0$ mode behaves strangely as in the 1.7-$M_\odot$ main-sequence models; the number of nodes decreases to 28 in the range $1.3 \lesssim B_{\rm p}^{0.25} \lesssim 1.5$.

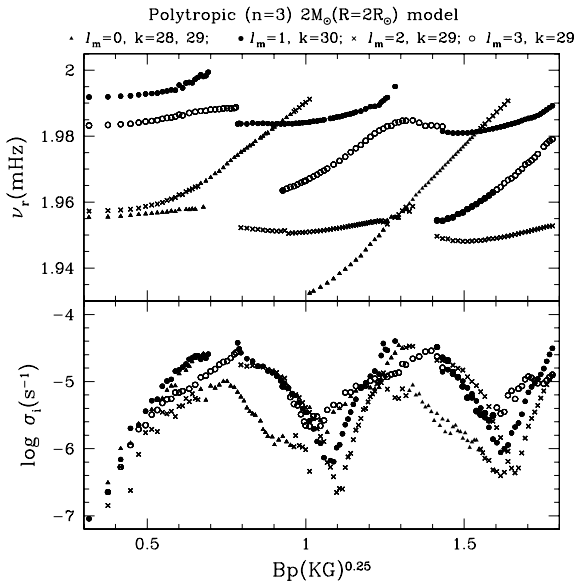

Figure 25. Eigenfrequencies versus $B_{\rm p}^{0.25}$ for some high-order p-modes of even and odd degrees of an $n = 3$ polytropic model star of mass 2 $M_\odot$ and radius 2 $R_\odot$. The upper and lower panels show cyclic frequencies and damping rates, respectively.

Fig. 26 displays the frequency shifts of odd modes with respect to the function ν_0(mHz) $[B_{\rm p}$(kG)$]^{0.25}$. Large squares in Fig. 26 show the frequency shifts of various modes $(12 \leqslant k \leqslant 55)$ with $\ell_{\rm m} = 1$ at $B_{\rm p} = 1$ kG. Other symbols in Fig. 26 show the frequency shifts with respect to the magnetic field strength for $(\ell_{\rm m}, k) = (1, 30)$ ($\nu_0 = 1.991$ mHz) and (3, 29) ($\nu_0 = 1.983$ mHz). The effect of magnetic fields on the pulsations of a polytrope is well scaled by $\nu_0 B_{\rm p}^{\alpha}$, where $\alpha = 1/(n + 1)$ with n being a polytropic index (Roberts & Soward 1983; Campbell & Papaloizou 1986; Cunha & Gough 2000).

Our results presented in Fig. 26 qualitatively agree well with the results of Cunha & Gough (2000) who approached the problem from a completely different angle. Hence, we are confident that the cyclic variation of the frequency shifts and of the damping rates are real (i.e. inherent to the physics of the problem). Fig. 26 indicates that jumps in frequency shifts at local maxima of the damping rates occur around ν_0(mHz)$[B_{\rm p}$(kG)$]^{0.25} = 1.5$ and 2.8. The data hint, furthermore, at another jump at around 3.7. These numbers agree very well with fig. 3 in Cunha & Gough (2000) for $B_{\rm p} = 1$ kG. The positions at local minima of the damping rates also agree well with their results.

The first frequency jumps in $\Delta\nu_{\rm r}$ measured by extrapolation in Fig. 26 amount roughly to ~ 20 μHz for the $\ell_{\rm m} = 1$ modes and to about 30 μHz for the $\ell_{\rm m} = 3$ mode. These numbers translate into $\Delta\omega_{\rm r}$ jumps of about 0.4 and 0.6, respectively, which are comparable to the values for the 1.7-$M_\odot$ main-sequence star models (Figs 12 and 13). On the other hand, fig. 3 in Cunha & Gough (2000) indicates that the first frequency jumps are about 27 μHz and 40 μHz for $\ell = 1$ and $\ell = 3$ modes, respectively. Our frequency jumps are about

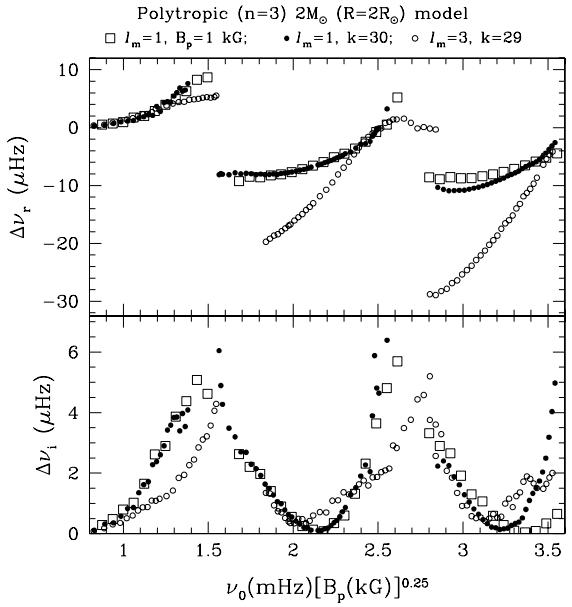

Figure 26. Frequency shifts for the odd modes shown in Fig. 25 and for various dipole overtone modes at a fixed field strength of 1 kG (big squares) as a functions of $\nu_0 B_{\rm p}^{0.25}$. The upper and lower panels show the real and imaginary parts, respectively, of the cyclic-frequency shift, $\Delta\nu = \nu(B_{\rm p}) - \nu_0$.

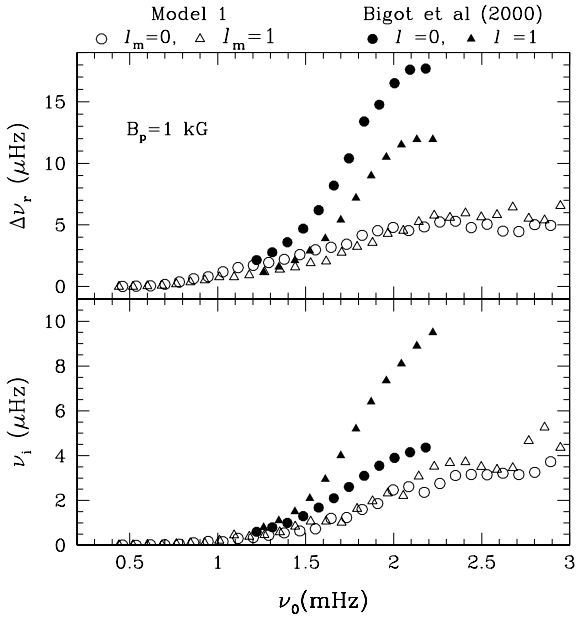

Figure 27. Comparison of frequency shifts at $B_{\rm p} = 1$ kG for $\ell_{\rm m} = 0$ and 1 modes with those obtained by Bigot et al. (2000). Open symbols are for our results of Model 1 and filled ones for the data taken from fig. 2 in Bigot et al. (2000).

30 per cent smaller than those of Cunha & Gough for both the $\ell_{\rm m} = 1$ and 3 cases, although the ratio of the frequency jump for $\ell_{\rm m} = 1$ to that for $\ell_{\rm m} = 3$ agrees well with that of Cunha & Gough. The reason for the discrepancy is unclear, though it may be related to the fact that the kinetic energy of pulsation is distributed broadly among ℓ-components when the damping rate is large.

The magnitude of the imaginary part $\nu_{\rm i}$ at a local maximum is uncertain; we may say that it certainly exceeds 6 μHz in the $\ell_{\rm m} = 1$ case, and 5 μHz in the $\ell_{\rm m} = 3$ case. Cunha & Gough's values of the first peak of $\nu_{\rm i}$ amount to about 10 μHz and 3 μHz for $\ell = 1$ and $\ell = 3$ modes, respectively, which are more or less consistent with our results.

We note that jumps in the frequency shift or local maxima of the damping rate for a given overtone mode of a polytrope occur at lower magnetic field strengths than in realistic main-sequence models. This property can be attributed to the density inversion in the hydrogen ionization zone (see Fig. 2). Exterior to the density inversion, η, which controls the effect of magnetic fields, is smaller for a given $B_{\rm p}$ in the realistic model than in the polytropic model. Therefore, to have a comparable magnetic effect, the magnetic field in a realistic model must be stronger than in a polytropic model with similar structure.

6.1.2 Zero-age main-sequence models

Dziembowski & Goode (1996) and Bigot et al. (2000) obtained eigenfrequencies of high-order p-modes in the presence of a dipole magnetic field for a main-sequence model. The magnetic field strength they considered ranges from $B_{\rm p} = 0.5$ kG to 1.5 kG. They expanded eigenfunctions into a series of spherical harmonics like in our method. Fig. 27 compares our frequency shifts for $\ell_{\rm m} = 0$ and 1 at $B_{\rm p} = 1$ kG with those obtained by Bigot et al. (2000) for their ZAMS model of $M = 1.8\ {\rm M}_\odot$ and $R = 1.531\ {\rm R}_\odot$. Since the parameters of their model are similar to those of our Model 1, cyclic frequencies in physical units are compared in Fig. 27.

For the frequency range $\nu_0 \lesssim 1.5$ mHz, our results agree well with those of Bigot et al. (2000). On the other hand, for the range $\nu_0 \gtrsim 1.5$ mHz, the frequency shifts of Bigot et al. are considerably higher than our results. The discrepancy could be partially attributed to a difference in mode identification adopted. We identified modes via the ℓ-component that has the largest kinetic energy in the truncated expansion series; e.g. for an $\ell_{\rm m} = 1$ mode the kinetic energy in the $\ell = 1$ component is largest among other ℓ-components included in the expansion. On the other hand, this seems not always to be the case in the analyses of Dziembowski & Goode (1996) and Bigot et al. (2000). Fig. 8 indicates that frequencies of $\ell_{\rm m} = 0$ modes are not far from those of $\ell_{\rm m} = 2$ modes around $B_{\rm p} \sim 1$ kG. Therefore, the $\ell = 0$ sequence of Bigot et al. in Fig. 27 might correspond to our $\ell_{\rm m} = 2$ modes for $\nu_0 \gtrsim 1.5$ mHz, which would result in higher $\Delta\omega_{\rm r}$s.

In addition, we note that their mechanical outer boundary condition allows a leakage of pulsation energy through an equatorial part of the outer boundary. This brings additional damping which is not included in our analysis. The additional damping may partially explain the fact that the imaginary part of the eigenfrequency of Bigot et al. (2000) is systematically higher than ours.

The frequency shifts shown in Fig. 27 increase monotonically with ν_0, which indicates that the range of ν_0 and $B_{\rm p}$ considered by Dziembowski & Goode (1996) and Bigot et al. (2000) is still on the low magnetic-field side of the first damping peak in the $B_{\rm p}$–frequency diagram (see Figs 10 and 11). A jump in $\Delta\nu_{\rm r}$ should appear for a higher value of $B_{\rm p}$. In this sense, the results of Dziembowski & Goode (1996) and Bigot et al. (2000) may not be so different from the results of Cunha & Gough (2000), because a jump in the frequency shift occurs at lower $B_{\rm p}$ or/and lower ν_0 for a polytrope than for a realistic model due to its superficial density inversion.

6.2 Magnetic selection of roAp oscillations

Let us compare the damping rates effected by the running slow waves with the growth rates of high-order p-modes excited by the κ-mechanism in the hydrogen ionization zone in the absence of a magnetic field. Gautschy et al. (1998) found that high-order p-modes of $\ell = 1$ are excited. Low-order modes, on the other hand, are stable if the star has a temperature inversion *and* a helium-depleted superficial layer. The typical value of the growth rate is $\approx 5 \times 10^{-6}$ s^{-1} ($\omega_{\rm i} \approx -0.02$) for a weak temperature inversion. (The growth rate is smaller if the magnitude of the temperature inversion and/or the abundance inhomogeneity is very small, as expected in the equatorial region of roAp stars.) Excitation with a growth rate similar to the above typical rate is suppressed by an energy drainage of magnetic slow waves if $\omega_{\rm i} \gtrsim 0.02$. According to Figs 12 and 13 classical κ-mechanism excitation of high-frequency modes can survive only if $f_{0.7} \lesssim 25$, $80 \lesssim f_{0.7} \lesssim 110$, and $170 \lesssim f_{0.7} \lesssim 200$ for $\ell_{\rm m} = 1$. For the survival of the overstability of $\ell_{\rm m} = 3$ modes under the influence of a magnetic field, roughly the same ranges of $f_{0.7}$ apply. Since there are some ambiguities in the mode identification in $\ell_{\rm m} = 0$ modes, we have not produced an $f_{0.7}$–$\Delta\omega$ diagram for even modes. A comparison between Figs 7 and 8 shows that the same ranges of $f_{0.7}$ apply even for $\ell_{\rm m} = 2$ modes. For $\ell_{\rm m} = 0$ modes (and $\ell_{\rm m} = 2$ modes with a large contribution from the $\ell = 0$ component), however, the damping rate between the first and the second damping minima are considerably smaller than the other cases. Therefore, for these modes the relative importance between the magnetic damping and the κ-mechanism excitation is marginal in the range $110 \lesssim f_{0.7} \lesssim 170$.

For $B_{\rm p} \gtrsim 1$ kG, the parameter range $f_{0.7} \lesssim 25$ corresponds to relatively low-order p-modes, for which the similarity parameter $f_{0.7}$ is inadequate. For a magnetic field strength of a few kG, the pulsation frequencies that lie within the 'window' of $80 \lesssim f_{0.7} \lesssim 110$ are comparable to those observed in the roAp stars, as discussed in Saio & Gautschy (2003). Thus, the damping due to the magnetic slow waves is expected to play a significant role in selecting modes.

Recently, Balmforth et al. (2001) proposed another avenue towards excitation of high-frequency oscillations in roAp stars. In their picture, convection is assumed to be suppressed in polar regions. Consequently, net driving by the κ-mechanism is very efficient in the polar regions where convective damping is absent. In the equatorial zones, on the other hand, damping exceeds the κ-mechanism driving. The overall stability of an oscillation mode depends then on the relative size of the driving polar regions and on the spherical 'quantum numbers' ℓ and m of the oscillation. From figures in Balmforth et al. (2001), we estimate the stability properties of high-frequency oscillations with frequency $\nu \approx 1.5$ mHz as follows. If the angular radius, $\vartheta_{\rm p}$, of the polar regions is $\approx 30^\circ$, the growth rate reaches $\approx 3 \times 10^{-6}$ s^{-1} (and it rises to about 3×10^{-5} s^{-1} if $\vartheta_{\rm p} \approx 40^\circ$) for $(\ell, m) = (1, 0)$ and $(2, 0)$ modes. Radial modes appear to be stable if $\vartheta_{\rm p} \lesssim 40^\circ$.

For an angular radius $\vartheta_{\rm p} = 30^\circ$ of the polar region, the expected growth rate for $\ell = 1$ and 2 modes is comparable to the magnitudes found by Gautschy et al. (1998) so that the effect of the magnetic damping is as discussed before. The only difference is that radial modes are stable according to the picture of Balmforth et al. If $\vartheta_{\rm p} \approx 40^\circ$ or bigger, the effect of magnetic damping is smaller than the driving by the κ-mechanism in most cases. However, a total suppression of convection in polar regions as extended as $\vartheta_{\rm p} \approx 40^\circ$ appears extreme. Consulting the diagrams shown in Balmforth et al. (2001) and Cunha (2002) for the magnetic stability effect on convection imparts the impression that convection is fully suppressed in considerably smaller-sized polar regions in most roAp stars. In the light of all the uncertainties in even qualitatively estimating the effects in hydromagnetic convection, we currently conclude that the damping effect due to magnetic slow waves plays an important role in selecting oscillation modes in roAp stars.

ACKNOWLEDGMENTS

Both authors are indebted to Prof E. A. Dorfi and the Sternwarte der Universität Wien for hospitality and for letting us stay at the Institute, thereby giving us the opportunity for intensive discussions that were necessary to finish this project successfully. We are grateful to Margarida Cunha and Don Kurtz for useful comments on a draft of this paper. This research has made use of NASA's Astrophysical Data System literature service.

REFERENCES

Bagnulo S., Landolfi M., Landi Degl'Innocenti M., 1999, A&A, 343, 865
Balmforth N. J., Cunha M. S., Dolez N., Gough D. O., Vauclair S., 2001, MNRAS, 323, 362
Balona L. A., Zima W., 2002, MNRAS, 336, 873
Bigot L., Dziembowski W. A., 2002, A&A, 391, 235
Bigot L., Provost J., Berthomieu G., Dziembowski W. A., Goode P. R., 2000, A&A, 356, 218
Biront D., Goossens M., Cousens A., Mestel L., 1982, MNRAS, 201, 619
Bogdan T. J., Cally P. S., 1997, Proc. R. Soc. Lond. A, 453, 943
Cally P. S., Bogdan T. J., 1993, MNRAS, 402, 721
Campbell C. G., Papaloizou J. C. B., 1986, MNRAS, 220, 577
Cox J. P., 1980, Theory of Stellar Pulsation. Princeton Univ. Press, Princeton
Cunha M. S., 2002, MNRAS, 333, 47
Cunha M. S., Gough D. O., 2000, MNRAS, 319, 1020
Dolez N., Gough D. O., 1982, in Cox J. P., Hansen C. J., eds, Pulsations in Classical and Cataclysmic Variable Stars, JILA, Boulder, CO, p. 248
Dziembowski W. A., Goode P. R., 1996, ApJ, 458, 338
Gautschy A., Saio H., Harzenmoser H., 1998, MNRAS, 301, 31
Iglesias C. A., Rogers R. J., 1996, ApJ, 464, 943
Kochukhov O., Ryabchikova T., 2001a, A&A, 374, 615
Kochukhov O., Ryabchikova T., 2001b, A&A, 377, L22
Kochukhov O., Landstreet J. D., Ryabchikova T., Weiss W. W., Kupka F., 2002, MNRAS, 337, L1
Kurtz D. W., 1982, MNRAS, 200, 807
Kurtz D. W., 1990, ARA&A, 28, 607
Kurtz D. W., 2000, in Berger M., Montgomery M. H., eds, ASP Conf Ser. Vol. 210, Delta Scuti and Related Stars. Astron. Soc. Pac., San Francisco, p. 287
Kurtz D. W., Shibahashi H., 1986, MNRAS, 223, 557
Kurtz D. W., Martinez P., Koen C., Sullivan D. J., 1996, MNRAS, 281, 883
Kurtz D. W., van Wyk, F., Roberts G., Marang F., Handler G., Medupe R., Kilkenny D., 1997, MNRAS, 287, 69
Malanushenko V., Savanov I., Ryabchikova T., 1998, Inf. Bull. Variable Stars, No. 4650
Martinez P., Kurtz D., 1994, MNRAS, 282, 243
Matthews J. M., 1991, PASP, 103, 5
Messiah A., 1961, Quantum Mechanics. North-Holland, Amsterdam
Roberts P. H., Soward A., 1983, MNRAS, 205, 1171
Saio H., Gautschy A., 2003, in Balona L. A., Henrichs H., Medupe T., eds, ASP Conf. Ser. Vol. 305, International Conference on Magnetic Fields in O, B and A Stars. Astron. Soc. Pac., San Francisco, p. 140
Shibahashi H., Takata M., 1993, PASJ, 45, 617
Spruit H. C., Bogdan T. J., 1992, ApJ, 391, L109
Takata M., Shibahashi H., 1995, PASJ, 47, 219
Unno W., Osaki Y., Ando H., Saio H., Shibahashi H., 1989, Nonradial Oscillations of Stars. Univ. of Tokyo Press, Tokyo

APPENDIX A: LOCAL ANALYSIS

To facilitate the understanding of the oscillation modes inherent in the MHD wave equations, we discuss their local properties in this appendix. To keep the analysis simple, the gas is taken as an ideal gas and the structure is assumed to be plane-parallel with a constant gravitational acceleration $\boldsymbol{g} = -g\boldsymbol{e}_z$. The unperturbed magnetic field is set to be uniform:

$$\boldsymbol{B}_0 = B_z\boldsymbol{e}_z + B_x\boldsymbol{e}_x. \tag{A1}$$

The displacement vector is decomposed as

$$\boldsymbol{\xi} = \xi_x(x, z)\boldsymbol{e}_x + \xi_z(x, z)\boldsymbol{e}_z, \tag{A2}$$

which corresponds to axisymmetric modes.

With the above assumptions, equations (2)–(5) are reduced to

$$\frac{\partial p'}{\partial z} + \frac{g}{c_s^2}p' = \rho(\sigma^2 - N^2)\xi_z - \frac{B_x}{4\pi}(B_z\nabla^2\xi_x - B_x\nabla^2\xi_z), \tag{A3}$$

$$\frac{\partial p'}{\partial x} = \sigma^2\rho\xi_x + \frac{B_z}{4\pi}(B_z\nabla^2\xi_x - B_x\nabla^2\xi_z) \tag{A4}$$

and

$$\frac{\partial \xi_z}{\partial z} - \frac{g}{c_s^2}\xi_z = -\frac{p'}{\Gamma_1 p} - \frac{\partial \xi_x}{\partial x}, \tag{A5}$$

where c_s is the sound speed, N is the Brunt–Väisälä frequency, and since we expect no variation in the y-direction, $\nabla^2 = (\partial^2/\partial x^2 + \partial^2/\partial z^2)$.

In addition to writing the horizontal variation of the perturbed quantities as $\exp(\mathrm{i}k_x x)$, we write, introducing the short-wave approximation, the vertical variation as $\exp(\mathrm{i}k_z z)$; i.e. we write

$$\xi_z, \xi_x, p' \propto \exp(\mathrm{i}k_z z + \mathrm{i}k_x x) \quad \text{with} \quad k^2 \equiv k_x^2 + k_z^2. \tag{A6}$$

Substituting the above forms and assuming that $\exp(\mathrm{i}k_z z)$ varies faster than the equilibrium structure variations, we obtain

$$\left(\sigma^2 - N^2 - c_s^2k_z^2 - \frac{k^2B_x^2}{4\pi\rho}\right)\xi_z = \left(c_s^2k_xk_z - \frac{k^2B_xB_z}{4\pi\rho}\right)\xi_x \tag{A7}$$

$$\left(\sigma^2 - c_s^2k_x^2 - \frac{k^2B_z^2}{4\pi\rho}\right)\xi_x = \left(c_s^2k_xk_z - \frac{k^2B_zB_x}{4\pi\rho}\right)\xi_z. \tag{A8}$$

If the equilibrium magnetic field is vertical ($B_x = 0$), the radial pulsations ($k_x = 0$) decouple from the Alfvén waves. Non-radial pulsations, however, couple inevitably with Alfvén-type waves in the presence of a magnetic field. From equations (A7) and (A8) we obtain a characteristic equation for σ as

$$\sigma^4 - \sigma^2[N^2 + k^2(c_s^2 + v_A^2)] + \frac{c_s^2k^2}{4\pi\rho}(\boldsymbol{k}\cdot\boldsymbol{B})^2 + N^2\left(c_s^2k_x^2 + \frac{k^2B_z^2}{4\pi\rho}\right) = 0, \tag{A9}$$

where we used the definition of the Alfvén speed

$$v_A^2 \equiv \frac{B_z^2 + B_x^2}{4\pi\rho}. \tag{A10}$$

We consider the case

$$N^2 \ll \sigma^2 \sim k^2(c_s^2 + v_A^2), \tag{A11}$$

which is applicable for p-modes in our 1.7-$M_\odot$ models, except for near the outer boundary (see Fig. 1). Neglecting the terms proportional to N^2 in equation (A9) we obtain

$$\sigma^2 = \frac{k^2(c_s^2 + v_A^2)}{2}\left[1 \pm \sqrt{1 - \frac{c_s^2(\boldsymbol{k}\cdot\boldsymbol{B})^2}{\pi\rho k^2(c_s^2 + v_A^2)^2}}\right], \tag{A12}$$

If either $c_s^2 \gg v^2{}_A$ or $v_A^2 \gg c_s^2$, we have

$$\sigma^2 \simeq k^2\left(c_s^2 + v_A^2\right) \quad \text{and} \quad \sigma^2 \simeq \frac{c_s^2}{c_s^2 + v_A^2}\frac{(\boldsymbol{k}\cdot\boldsymbol{B})^2}{4\pi\rho}. \tag{A13}$$

The first and the second relations correspond to the fast and slow waves, respectively. The two types of waves cannot be separated clearly when $c_s \approx v_A$, indicating a strong coupling between those waves. The slow waves decouple from the p-mode in deeper layers where $c_s \gg v_A$ and have a local wavelength of about $2\pi v_A/\sigma$, much shorter than the wavelength of the p-mode $\sim 2\pi c_s/\sigma$.

APPENDIX B: TECHNICAL DETAILS OF THE EXPANSION METHOD

This appendix contains technical details of the expansion method for axisymmetric eigenmodes of stars with dipole magnetic fields.

B1 Set of equations

Using the variables defined in equation (11), equations (2)–(5) become

$$\frac{\mathrm{d}y_{1,\ell}}{\mathrm{d}\ln r} = \left(\frac{V}{\Gamma_1} - 3\right)y_{1,\ell} + \left[\frac{\ell(\ell+1)}{c_1\omega^2} - \frac{V}{\Gamma_1}\right]y_{2,\ell} + \frac{\ell(\ell+1)}{c_1\omega^2}y_{3,\ell} \tag{B1}$$

$$\frac{\mathrm{d}y_{2,\ell}}{\mathrm{d}\ln r} = c_1(\omega^2 - n^2)y_{1\ell} + (c_1n^2 - U + 1)y_{2,\ell} - \eta\left[\left(\frac{\mathrm{d}y_{4,\ell-1}}{\mathrm{d}\ln r} - 2y_{4,\ell-1} - \frac{x^3}{B_p}b_{r\ell-1}\right)(\ell-1)J_\ell - \left(\frac{\mathrm{d}y_{4,\ell+1}}{\mathrm{d}\ln r} - 2y_{4,\ell+1} - \frac{x^3}{B_p}b_{r\ell+1}\right)(\ell+2)J_{\ell+1}\right] \tag{B2}$$

$$\ell(\ell+1)y_{3,\ell} = -2\eta\left[\left(\frac{\mathrm{d}y_{4,\ell-1}}{\mathrm{d}\ln r} - 2y_{4,\ell-1} - \frac{x^3}{B_p}b_{r\ell-1}\right)(\ell^2-1)J_\ell + \left(\frac{\mathrm{d}y_{4,\ell+1}}{\mathrm{d}\ln r} - 2y_{4,\ell+1} - \frac{x^3}{B_p}b_{r,\ell+1}\right)\ell(\ell+2)J_{\ell+1}\right] \tag{B3}$$

$$\frac{x^3}{B_p}b_{r,\ell} = \frac{1}{2}[(\ell+1)J_\ell y_{1,\ell-1} - \ell J_{\ell+1}y_{1,\ell+1}] + \frac{(\ell^2-1)J_\ell}{c_1\omega^2}(y_{2,\ell-1} + y_{3,\ell-1}) + \frac{\ell(\ell+2)J_{\ell+1}}{c_1\omega^2}(y_{2,\ell+1} + y_{3,\ell+1}) \tag{B4}$$

$$\begin{aligned}\ell(\ell+1)y_{4,\ell} = {} & \left[\frac{V}{2\Gamma_1}(y_{1,\ell-1} - y_{2,\ell-1}) - 2y_{1,\ell-1}\right](\ell+1)J_\ell \\ & - \left[\frac{V}{2\Gamma_1}(y_{1,\ell+1} - y_{2,\ell+1}) - 2y_{1,\ell+1}\right]\ell J_{\ell+1} \\ & + (\ell^2-1)J_\ell\frac{\mathrm{d}}{\mathrm{d}\ln r}\left(\frac{y_{2,\ell-1} + y_{3,\ell-1}}{c_1\omega^2}\right) \\ & + \ell(\ell+2)J_{\ell+1}\frac{\mathrm{d}}{\mathrm{d}\ln r}\left(\frac{y_{2,\ell+1} + y_{3,\ell+1}}{c_1\omega^2}\right) \\ & + \frac{(\ell-2)(\ell^2-1)}{2c_1\omega^2}J_\ell(y_{2,\ell-1} + y_{3,\ell-1}) \\ & - \frac{\ell(\ell+2)(\ell+3)}{2c_1\omega^2}J_{\ell+1}(y_{2,\ell+1} + y_{3,\ell+1}),\end{aligned} \tag{B5}$$

where

$$c_1 = \frac{r^3}{R^3}\frac{M}{M_r}, \quad V = \frac{g\rho r}{p}, \quad U = \frac{4\pi r^3 \rho}{M_r},$$
$$n^2 = N^2\frac{R^3}{GM}, \quad J_\ell = \frac{\ell}{\sqrt{4\ell^2-1}}. \tag{B6}$$

Define the following vectors:

$$\boldsymbol{Y}_i : \begin{cases} Y_i^j = y_{i,\ell_j} & \text{for} \quad i = 1, 2, 3 \\ Y_4^j = y_{4,\ell_j+1} \end{cases} \tag{B7}$$

with $j = 1, 2, \ldots$ and ℓ_j defined as

$$\ell_j = \begin{cases} 2j-1 & \text{for odd modes,} \\ 2j-2 & \text{for even modes.} \end{cases} \tag{B8}$$

Then, equation (B1) can be written as

$$\frac{\mathrm{d}\boldsymbol{Y}_1}{\mathrm{d}\ln r} = \left(\frac{V}{\Gamma_1} - 3\right)\boldsymbol{Y}_1 + \left(\frac{\boldsymbol{\Lambda}}{c_1\omega^2} - \frac{V}{\Gamma_1}\right)\boldsymbol{Y}_2 + \frac{\boldsymbol{\Lambda}}{c_1\omega^2}\boldsymbol{Y}_3, \tag{B9}$$

where $\boldsymbol{\Lambda}$ is a diagonal matrix defined as

$$\Lambda_{jj} = \ell_j(\ell_j+1). \tag{B10}$$

Equation (B2) becomes

$$\frac{\mathrm{d}\boldsymbol{Y}_2}{\mathrm{d}\ln r} = c_1(\omega^2 - n^2)\boldsymbol{Y}_1 + (c_1 n^2 - U + 1)\boldsymbol{Y}_2 + \eta\boldsymbol{H}\left(\frac{\mathrm{d}\boldsymbol{Y}_4}{\mathrm{d}\ln r} - 2\boldsymbol{Y}_4 - \boldsymbol{B}_R\right), \tag{B11}$$

where $\boldsymbol{B}_R$ is a vector defined as

$$B_R^j = \frac{x^3 b_{r\ell_j+1}}{B_\mathrm{p}} \tag{B12}$$

and the matrix $\boldsymbol{H}$ has the elements

$$H_{jj} = (\ell_j+2)J_{\ell_j+1}, \quad H_{jj-1} = -(\ell_j-1)J_{\ell_j}, \tag{B13}$$

and the other elements are zero. Equation (B3) can be written as

$$\boldsymbol{\Lambda}\boldsymbol{Y}_3 = -2\eta\boldsymbol{M}\left(\frac{\mathrm{d}\boldsymbol{Y}_4}{\mathrm{d}\ln r} - 2\boldsymbol{Y}_4 - \boldsymbol{B}_R\right) \tag{B14}$$

or

$$\frac{\mathrm{d}\boldsymbol{Y}_4}{\mathrm{d}\ln r} = 2\boldsymbol{Y}_4 + \boldsymbol{B}_R - \frac{1}{2\eta}\boldsymbol{M}^{-1}\boldsymbol{\Lambda}\boldsymbol{Y}_3, \tag{B15}$$

where

$$M_{jj} = \ell_j(\ell_j+2)J_{\ell_j+1}, \quad M_{jj-1} = (\ell_j^2-1)J_{\ell_j}, \tag{B16}$$

and the other elements are zero. After using equation (B15) in equation (B11) we have

$$\frac{\mathrm{d}\boldsymbol{Y}_2}{\mathrm{d}\ln r} = c_1(\omega^2 - n^2)\boldsymbol{Y}_1 + (c_1 n^2 - U + 1)\boldsymbol{Y}_2 - \frac{1}{2}\boldsymbol{H}\boldsymbol{M}^{-1}\boldsymbol{\Lambda}Y_3. \tag{B17}$$

Equation (B4) may be written as

$$\boldsymbol{B}_R = \frac{1}{2}\boldsymbol{W}Y_1 + \frac{1}{c_1\omega^2}\boldsymbol{Q}(\boldsymbol{Y}_2 + \boldsymbol{Y}_3), \tag{B18}$$

with

$$W_{jj} = (\ell_j+2)J_{\ell_j+1}, \quad W_{jj+1} = -(\ell_j+1)J_{\ell_j+2}, \tag{B19}$$

the other elements being zero, and

$$Q_{jj} = (\ell_j+2)\ell_j J_{\ell_j+1}, \quad Q_{jj+1} = (\ell_j+1)(\ell_j+3)J_{\ell_j+2}, \tag{B20}$$

with the other elements being zero. Using equation (B18) in (B15) leads to

$$\frac{\mathrm{d}\boldsymbol{Y}_4}{\mathrm{d}\ln r} = \frac{\boldsymbol{W}}{2}\boldsymbol{Y}_1 + \frac{\boldsymbol{Q}}{c_1\omega^2}\boldsymbol{Y}_2 + \left(\frac{\boldsymbol{Q}}{c_1\omega^2} - \frac{1}{2\eta}\boldsymbol{M}^{-1}\boldsymbol{\Lambda}\right)\boldsymbol{Y}_3 + 2\boldsymbol{Y}_4. \tag{B21}$$

Equation (B5) may be written as

$$\boldsymbol{\Lambda}^+\boldsymbol{Y}_4 = \boldsymbol{W}\left[\left(\frac{V}{2\Gamma_1} - 2\right)\boldsymbol{Y}_1 - \frac{V}{2\Gamma_1}\boldsymbol{Y}_2\right] - \frac{1}{c_1\omega^2}\left[\frac{1}{2}\boldsymbol{S} + (3-U)\boldsymbol{Q}\right](\boldsymbol{Y}_2 + \boldsymbol{Y}_3) + \frac{\boldsymbol{Q}}{c_1\omega^2}\left(\frac{\mathrm{d}\boldsymbol{Y}_2}{\mathrm{d}\ln r} + \frac{\mathrm{d}\boldsymbol{Y}_3}{\mathrm{d}\ln r}\right), \tag{B22}$$

where

$$S_{jj} = -(\ell_j-1)\ell_j(\ell_j+2)J_{\ell_j+1},$$
$$S_{jj+1} = (\ell_j+1)(\ell_j+3)(\ell_j+4)J_{\ell_j+2}, \tag{B23}$$

the other elements are zero, and $\boldsymbol{\Lambda}^+$ is diagonal with

$$\Lambda^+_{jj} = (\ell_j+1)(\ell_j+2). \tag{B24}$$

After using the right-hand side of equation (B17) in (B22) we obtain

$$\frac{\mathrm{d}\boldsymbol{Y}_3}{\mathrm{d}\ln r} = \left[c_1\omega^2\left(2 - \frac{V}{2\Gamma_1}\right)\boldsymbol{Q}^{-1}\boldsymbol{W} + (n^2-\omega^2)c_1\right]\boldsymbol{Y}_1 + \left[c_1\omega^2\frac{V}{2\Gamma_1}\boldsymbol{Q}^{-1}\boldsymbol{W} + \frac{1}{2}\boldsymbol{Q}^{-1}\boldsymbol{S} + 2 - c_1 n^2\right]\boldsymbol{Y}_2 + \left[3 - U + \frac{1}{2}\left(\boldsymbol{Q}^{-1}\boldsymbol{S} + \boldsymbol{H}\boldsymbol{M}^{-1}\boldsymbol{\Lambda}\right)\right]\boldsymbol{Y}_3 + c_1\omega^2\boldsymbol{Q}^{-1}\boldsymbol{\Lambda}^+\boldsymbol{Y}_4 \tag{B25}$$

B2 Boundary conditions

B2.1 The mechanical outer boundary condition

According to Cox (1980), we adopt the mechanical outer boundary condition based on the requirement

$$\frac{\partial}{\partial r}\left(\frac{\delta p}{p}\right) \text{ remains finite when } p \longrightarrow 0. \tag{B26}$$

Using this requirement in the radial component of the momentum equation under the Cowling approximation leads to

$$V(y_{2,\ell} - y_{1,\ell}) = \frac{\ell(\ell+1)}{c_1\omega^2}(y_{2,\ell} + y_{3,\ell}) - (c_1\omega^2 + 4)y_{1,\ell}. \tag{B27}$$

The effect of the Lorentz force does not appear in the above equation because the magnetic field is assumed to be rotation-free at the surface (Section B2.2).

Using vector variables $\boldsymbol{Y}_j$, we have

$$(V - c_1\omega^2 - 4)\boldsymbol{Y}_1 - \left(V - \frac{\boldsymbol{\Lambda}}{c_1\omega^2}\right)\boldsymbol{Y}_2 + \frac{\boldsymbol{\Lambda}}{c_1\omega^2}\boldsymbol{Y}_3 = 0. \tag{B28}$$

Note that this condition coincides with the zero boundary condition of $\delta p = 0$ in the limit of $V \longrightarrow \infty$.

B2.2 The magnetic outer boundary condition

The perturbed magnetic field $\boldsymbol{B}'$ at the outer boundary must connect continuously to the vacuum field which is rotation-free, i.e. $\nabla \times \boldsymbol{B}' = 0$. Therefore, $\boldsymbol{B}'$ is a potential field, so that

$$\boldsymbol{B}' = \nabla\Psi. \tag{B29}$$

With $\nabla \cdot \boldsymbol{B}' = 0$ we arrive at

$$\nabla^2\Psi = 0. \tag{B30}$$

The angular dependence of the potential Ψ is expanded as

$$\Psi = \sum_{\ell\geqslant 0} \Psi_\ell(r) Y_\ell^0. \tag{B31}$$

Equation (B30) becomes

$$\frac{\mathrm{d}}{\mathrm{d}r}\left(r^2\frac{\mathrm{d}\Psi_\ell}{\mathrm{d}r}\right) = \ell(\ell+1)\Psi_\ell, \tag{B32}$$

which is satisfied if $\Psi \propto r^\ell$ or $\propto r^{-(\ell+1)}$. Requiring the solution to remain finite at infinity, we can write

$$\Psi = \sum_{\ell\geqslant 0} \frac{E_\ell}{r^{\ell+1}} Y_\ell^0. \tag{B33}$$

Substituting this into equation (B29) leads to

$$\boldsymbol{B}' = \sum_{\ell\geqslant 0}\left[-(\ell+1)\frac{E_\ell}{r^{\ell+2}}Y_\ell^0\boldsymbol{e}_r + \frac{E_\ell}{r^{\ell+1}}\nabla Y_\ell^0\right]. \tag{B34}$$

Comparing this equation with (9) gives

$$b_{r\ell} = -(\ell+1)\frac{E_\ell}{r^{\ell+2}} \quad \text{and} \quad b_{p\ell} = \frac{E_\ell}{r^{\ell+2}}. \tag{B35}$$

Combining these two relations leads to

$$b_{r\ell} + (\ell+1)b_{p\ell} = 0. \tag{B36}$$

Using vector variables, equation (B36) can be rewritten as

$$\boldsymbol{B}_R + \boldsymbol{L}^+\boldsymbol{Y}_4 = 0, \tag{B37}$$

where $\boldsymbol{L}^+$ is a diagonal matrix defined by

$$L^+_{jj} = \ell_j + 2. \tag{B38}$$

Finally, using equation (B18) we arrive at

$$\frac{1}{2}\boldsymbol{W}Y_1 + \frac{1}{c_1\omega^2}\boldsymbol{Q}(\boldsymbol{Y}_2 + \boldsymbol{Y}_3) + \boldsymbol{L}^+\boldsymbol{Y}_4 = 0. \tag{B39}$$

B2.3 The central mechanical boundary condition

Near the centre, the magnetic effects are negligible and a boundary condition for non-radial pulsations without magnetic field

$$c_1\omega^2 y_{1,\ell} - \ell y_{2,\ell} = 0 \tag{B40}$$

is applicable. Using vector variables, the last equation reads as

$$c_1\omega^2\boldsymbol{Y}_1 - \boldsymbol{L}\boldsymbol{Y}_2 = 0, \tag{B41}$$

where $\boldsymbol{L}$ is a diagonal matrix defined as

$$L_{jj} = \ell_j. \tag{B42}$$

B2.4 The inner magnetic boundary condition in the envelope

For our analysis, we divide the stellar interior into two regions: the thin outer zone is the one affected appreciably by the magnetic field, whereas it is unimportant in the inner zone. Hence, in the inner part we solve only equations (B9) and (B17) and set $\boldsymbol{Y}_3 \equiv 0$; these are the same equations as for adiabatic non-radial pulsations without a magnetic field. Because of the effects of the magnetic field in the outer zone, the perturbation variables are, however, complex. In the outer zone, we solve the full set of equations (B9), (B17), (B25) and (B21). Since we do not solve the last two equations in the inner zone, we have to impose boundary conditions for $\boldsymbol{Y}_3$ and $\boldsymbol{Y}_4$ at the base of the outer zone. We formulate running wave conditions based on the assumption of inwardly propagating slow magnetic waves which oscillate spatially very rapidly and which dissipate before being reflected at the stellar centre.

The rapid oscillation of the magnetic variables ensures the following relation:

$$\left|\frac{\mathrm{d}\boldsymbol{Y}_3}{\mathrm{d}\ln r}\right| \gg |\boldsymbol{Y}_3|, \qquad \left|\frac{\mathrm{d}\boldsymbol{Y}_4}{\mathrm{d}\ln r}\right| \gg |\boldsymbol{Y}_4|. \tag{B43}$$

Therefore, equations (B25) and (B21) can be approximated by

$$\frac{\mathrm{d}\boldsymbol{Y}_3}{\mathrm{d}\ln r} \simeq +c_1\omega^2\boldsymbol{Q}^{-1}\boldsymbol{\Lambda}^+\boldsymbol{Y}_4 + \boldsymbol{F}_1 \tag{B44}$$

and

$$\frac{\mathrm{d}\boldsymbol{Y}_4}{\mathrm{d}\ln r} \simeq -\frac{1}{2\eta}\boldsymbol{M}^{-1}\boldsymbol{\Lambda}\boldsymbol{Y}_3 + \boldsymbol{F}_2, \tag{B45}$$

where the vectors $\boldsymbol{F}_1$ and $\boldsymbol{F}_2$ defined as

$$\boldsymbol{F}_1 = \left[c_1\omega^2\left(2 - \frac{V}{2\Gamma_1}\right)\boldsymbol{Q}^{-1}\boldsymbol{W} + (n^2-\omega^2)c_1\right]\boldsymbol{Y}_1 + \left[c_1\omega^2\frac{V}{2\Gamma_1}\boldsymbol{Q}^{-1}\boldsymbol{W} + \frac{1}{2}\boldsymbol{Q}^{-1}\boldsymbol{S} + 2 - c_1n^2\right]\boldsymbol{Y}_2, \tag{B46}$$

and

$$\boldsymbol{F}_2 = \frac{\boldsymbol{W}}{2}\boldsymbol{Y}_1 + \frac{\boldsymbol{Q}}{c_1\omega^2}\boldsymbol{Y}_2 \tag{B47}$$

are assumed to be constant near the boundary.

In the following, we consider vectors $\boldsymbol{Y}_i$ that are truncated after the first J elements. Define now vectors $\boldsymbol{Z}$ and $\boldsymbol{F}$ with $2J$ elements such as

$$\boldsymbol{Z} = \begin{pmatrix}\boldsymbol{Y}_3\\ \boldsymbol{Y}_4\end{pmatrix}, \qquad \boldsymbol{F} = \begin{pmatrix}\boldsymbol{F}_1\\ \boldsymbol{F}_2\end{pmatrix}. \tag{B48}$$

Then, equations (B44) and (B45) become

$$\frac{\mathrm{d}\boldsymbol{Z}}{\mathrm{d}\ln r} = \boldsymbol{A}\boldsymbol{Z} + \boldsymbol{F}, \tag{B49}$$

where $\boldsymbol{A}$ is a $2J \times 2J$ matrix defined as

$$\boldsymbol{A} = \begin{pmatrix}\boldsymbol{0} & c_1\omega^2\boldsymbol{Q}^{-1}\boldsymbol{\Lambda}^+\\ -\frac{1}{2\eta}\boldsymbol{M}^{-1}\boldsymbol{\Lambda} & \boldsymbol{0}\end{pmatrix}. \tag{B50}$$

Let the eigenvalues of matrix $\boldsymbol{A}$ be $\mathrm{i}k_j$ and the corresponding eigenvectors be $\boldsymbol{u}_j$ ($j = 1, 2, \ldots, 2J$), so that solutions of the homogeneous equation which is equation (B49) without $\boldsymbol{F}$ are written as

$$\hat{\boldsymbol{Z}} = C_1\boldsymbol{u}_1\mathrm{e}^{\mathrm{i}k_1\ln r} + \cdots + C_{2J}\boldsymbol{u}_{2J}\mathrm{e}^{\mathrm{i}k_{2J}\ln r}. \tag{B51}$$

The set of eigenvalues consists of J solutions of inward ($\Re(k) > 0$) propagating waves and J solutions of outward ($\Re(k) < 0$) propagating waves. Since we consider only waves that propagate inwards,

we use only those solutions with positive real parts. Let these eigenvalues be $ik_1, \ldots, ik_J$ so that we can write

$$\hat{\boldsymbol{Z}} = C_1\boldsymbol{u}_1 e^{ik_1 \ln r} + \cdots + C_J\boldsymbol{u}_J e^{ik_J \ln r}. \tag{B52}$$

We split equation (B52) into two sets. Dividing $\boldsymbol{u}_j$ into an upper $\boldsymbol{u}_{ju}$ and a lower half $\boldsymbol{u}_{jl}$, we split $\boldsymbol{Z}$ into $\hat{\boldsymbol{Z}}_u = \boldsymbol{Y}_3$ and $\hat{\boldsymbol{Z}}_l = \boldsymbol{Y}_4$. Each of these vectors has J elements. Then, equation (B52) is divided into two equations

$$\hat{\boldsymbol{Z}}_u = C_1\boldsymbol{u}_{1u} e^{ik_1 \ln r} + \cdots + C_J\boldsymbol{u}_{Ju} e^{ik_J \ln r} \tag{B53}$$

$$\hat{\boldsymbol{Z}}_l = C_1\boldsymbol{u}_{1l} e^{ik_1 \ln r} + \cdots + C_J\boldsymbol{u}_{Jl} e^{ik_J \ln r}. \tag{B54}$$

By solving, say for the upper part (u), we obtain the relation

$$\begin{pmatrix} C_1 \exp(ik_1 \ln r) \\ \vdots \\ C_J \exp(ik_J \ln r) \end{pmatrix} = (\boldsymbol{u}_{1u}\boldsymbol{u}_{2u} \ldots \boldsymbol{u}_{Ju})^{-1} \hat{\boldsymbol{Z}}_u \tag{B55}$$

where $(\boldsymbol{u}_{1u}\boldsymbol{u}_{2u} \ldots \boldsymbol{u}_{Ju})$ is a $J \times J$ matrix composed of column vectors $\boldsymbol{u}_{ju}$. (If this matrix turns out to be singular, one can try to solve for the lower part (l) in equation (B54) instead. If this latter case leads to a singular matrix too, the splitting of equation B52 should be done differently.) Substituting equation (B55) into the appropriate part of equation (B54), we obtain

$$\hat{\boldsymbol{Z}}_l = (\boldsymbol{u}_{1l}\boldsymbol{u}_{2l} \ldots \boldsymbol{u}_{Jl})(\boldsymbol{u}_{1u}\boldsymbol{u}_{2u} \ldots \boldsymbol{u}_{Ju})^{-1} \hat{\boldsymbol{Z}}_u. \tag{B56}$$

Using the relation

$$\boldsymbol{Z} = \hat{\boldsymbol{Z}} - \boldsymbol{A}^{-1}\boldsymbol{F} \tag{B57}$$

in equation (B56), we obtain a set of linear relations between $\boldsymbol{Y}_3$ and $\boldsymbol{Y}_4$ which can be used as magnetic boundary conditions at the bottom of a star's thin superficial layer that is strongly magnetically influenced.

B3 Even modes

Since $\ell_1 = 0$ for even modes, the matrices $\boldsymbol{Q}^{-1}\boldsymbol{W}$ and $\boldsymbol{Q}^{-1}\boldsymbol{S}$ are singular. This can be avoided by using a different set of equations. Looking at equations (B1)–(B5), we notice that the $y_{3,\ell}$ always enter in the form $\ell\, y_{3,\ell}$. Therefore, y_{3,ℓ_1} need not be considered at all for even modes. Taking advantage of this fact, we can define

$$\overline{Y}_3^j \equiv (\ell_j + 2)(\ell_j + 3) y_{3,\ell_j+2}, \quad \text{with} \quad j = 1, 2, \ldots. \tag{B58}$$

For the rest, we use the vector variables defined earlier

$$Y_1^j = y_{1,\ell_j}, \quad Y_2^j = y_{2,\ell_j}, \quad \text{and} \quad Y_4^j = y_{4,\ell_j+1}, \tag{B59}$$

where $j = 1, 2, \ldots$, and

$$\ell_j = 2(j-1) \quad \text{forevenmodes;} \quad j = 1, 2, \ldots. \tag{B60}$$

Using the above vectors, equation (B1) may be cast in the form

$$\frac{\mathrm{d}\boldsymbol{Y}_1}{\mathrm{d}\ln r} = \left(\frac{V}{\Gamma_1} - 3\right)\boldsymbol{Y}_1 + \left[\frac{\boldsymbol{\Lambda}}{c_1\omega^2} - \frac{V}{\Gamma_1}\right]\boldsymbol{Y}_2 + \frac{\boldsymbol{D}}{c_1\omega^2}\overline{\boldsymbol{Y}}_3, \tag{B61}$$

where

$$D_{jj-1} = 1, \quad \text{with the other elements being zero.} \tag{B62}$$

Equation (B2) for $\boldsymbol{Y}_2$ remains unchanged. Equation (B3) becomes

$$\overline{\boldsymbol{Y}}_3 = -2\eta\overline{\boldsymbol{M}}\left(\frac{\mathrm{d}\boldsymbol{Y}_4}{\mathrm{d}\ln r} - 2\boldsymbol{Y}_4 - \boldsymbol{B}_R\right), \tag{B63}$$

where

$$\begin{aligned} \overline{M}_{jj} &= (\ell_j + 1)(\ell_j + 3) J_{\ell_j+2}, \\ \overline{M}_{jj+1} &= (\ell_j + 2)(\ell_j + 4) J_{\ell_j+3}, \end{aligned} \tag{B64}$$

with the other elements being zero. Equation (B4) can be written as

$$\boldsymbol{B}_R = \frac{1}{2}\boldsymbol{W}Y_1 + \frac{\boldsymbol{Q}}{c_1\omega^2}\boldsymbol{Y}_2 + \frac{\overline{\boldsymbol{Q}}}{c_1\omega^2}\overline{\boldsymbol{Y}}_3, \tag{B65}$$

where

$$\overline{Q}_{jj} = \frac{\ell_j + 1}{\ell_j + 2} J_{\ell_j+2}, \quad \overline{Q}_{jj-1} = \frac{\ell_j + 2}{\ell_j + 1} J_{\ell_j+1}, \tag{B66}$$

and the other elements being zero. From equation (B5) we arrive at

$$\begin{aligned} \boldsymbol{\Lambda}^+\boldsymbol{Y}_4 = \boldsymbol{W}&\left[\left(\frac{V}{2\Gamma_1} - 2\right)\boldsymbol{Y}_1 - \frac{V}{2\Gamma_1}\boldsymbol{Y}_2\right] \\ &+ \frac{\boldsymbol{Q}}{c_1\omega^2}\frac{\mathrm{d}\boldsymbol{Y}_2}{\mathrm{d}\ln r} + \frac{\overline{\boldsymbol{Q}}}{c_1\omega^2}\frac{\mathrm{d}\overline{\boldsymbol{Y}}_3}{\mathrm{d}\ln r} - \left[\frac{\boldsymbol{S}}{2} + (3-U)\boldsymbol{Q}\right]\frac{\boldsymbol{Y}_2}{c_1\omega^2} \\ &- \left[\frac{\overline{\boldsymbol{S}}}{2} + (3-U)\overline{\boldsymbol{Q}}\right]\frac{\overline{\boldsymbol{Y}}_3}{c_1\omega^2}, \end{aligned} \tag{B67}$$

where

$$\begin{aligned} \overline{S}_{jj} &= \frac{(\ell_j + 1)(\ell_j + 4)}{\ell_j + 2} J_{\ell_j+2}, \\ \overline{S}_{jj-1} &= -\frac{(\ell_j - 1)(\ell_j + 2)}{\ell_j + 1} J_{\ell_j+1}, \end{aligned} \tag{B68}$$

with the rest of the elements being zero. Substituting equation (B63) into (B11) leads to

$$\frac{\mathrm{d}\boldsymbol{Y}_2}{\mathrm{d}\ln r} = c_1(\omega^2 - n^2)\boldsymbol{Y}_1 + (c_1 n^2 - U + 1)\boldsymbol{Y}_2 - \frac{1}{2}\boldsymbol{H}\overline{\boldsymbol{M}}^{-1}\overline{\boldsymbol{Y}}_3. \tag{B69}$$

Combining equation (B63) with (B65) gives

$$\frac{\mathrm{d}\boldsymbol{Y}_4}{\mathrm{d}\ln r} = \frac{1}{2}\boldsymbol{W}Y_1 + \frac{\boldsymbol{Q}}{c_1\omega^2}\boldsymbol{Y}_2 + \left(\frac{\overline{\boldsymbol{Q}}}{c_1\omega^2} - \frac{1}{2\eta}\overline{\boldsymbol{M}}^{-1}\right)\overline{\boldsymbol{Y}}_3 + 2\boldsymbol{Y}_4. \tag{B70}$$

Substituting equation (B69) into equation (B67), we have

$$\begin{aligned} \frac{\mathrm{d}\overline{\boldsymbol{Y}}_3}{\mathrm{d}\ln r} = c_1\overline{\boldsymbol{Q}}^{-1}&\left[\omega^2\left(2 - \frac{V}{2\Gamma_1}\right)\boldsymbol{W} + (n^2 - \omega^2)\boldsymbol{Q}\right]\boldsymbol{Y}_1 \\ &+ \overline{\boldsymbol{Q}}^{-1}\left[c_1\omega^2\frac{V}{2\Gamma_1}\boldsymbol{W} + \left(\frac{\boldsymbol{S}}{2} + 2\boldsymbol{Q}\right) - c_1 n^2\boldsymbol{Q}\right]\boldsymbol{Y}_2 \\ &+ \left[3 - U + \frac{1}{2}\overline{\boldsymbol{Q}}^{-1}\left(\overline{\boldsymbol{S}} + \boldsymbol{Q}\boldsymbol{H}\overline{\boldsymbol{M}}^{-1}\right)\right]\overline{\boldsymbol{Y}}_3 \\ &+ c_1\omega^2\overline{\boldsymbol{Q}}^{-1}\boldsymbol{\Lambda}^+\boldsymbol{Y}_4. \end{aligned} \tag{B71}$$

The mechanical outer and central boundary conditions are the same as for the odd modes. The magnetic outer boundary condition is obtained from combining equation (B37) and (B65):

$$\frac{1}{2}\boldsymbol{W}Y_1 + \frac{\boldsymbol{Q}}{c_1\omega^2}\boldsymbol{Y}_2 + \frac{\overline{\boldsymbol{Q}}}{c_1\omega^2}\overline{\boldsymbol{Y}}_3 + \boldsymbol{L}^+\boldsymbol{Y}_4 = 0. \tag{B72}$$

For even modes, the magnetic boundary condition at the bottom of the magnetically dominated outer layer can be obtained by the same method as discussed for odd modes. Now, however, $\boldsymbol{Y}_3$ must be replaced by $\overline{\boldsymbol{Y}}_3$ and matrix $\boldsymbol{A}$ has to be replaced by $\boldsymbol{A}$:

$$\overline{\boldsymbol{A}} = \begin{pmatrix} \boldsymbol{0} & c_1\omega^2\overline{\boldsymbol{Q}}^{-1}\boldsymbol{\Lambda}^+ \\ -\frac{1}{2\eta}\overline{\boldsymbol{M}}^{-1} & \boldsymbol{0} \end{pmatrix}. \tag{B73}$$

This paper has been typeset from a TEX/LATEX file prepared by the author.